Journal of Materials Chemistry A

ROYAL SOCIETY OF CHEMISTRY

PAPER

Cite this: J. Mater. Chem. A, 2020, 8, 20513

Characterizing surface states in hematite nanorod photoanodes, both beneficial and detrimental to solar water splitting efficiency†

Dana Stanescu, *[a] Mekan Piriyev ,[b] Victoria Villard,[a] Cristian Mocuta, [b] Adrien Besson,[b] Dris Ihiawakrim, [c] Ovidiu Ersen, [c] Jocelyne Leroy, [d] Sorin G. Chiuzbaian,[e] Adam P. Hitchcock[f] and Stefan Stanescu *[b]

Received 3rd July 2020
Accepted 8th September 2020

DOI: 10.1039/d0ta06524b

rsc.li/materials-a

The performance of hematite and Ti-substituted hematite nanorods as photoanodes for solar water splitting was quantitatively evaluated from the photoelectrochemical point of view. The nanostructure, morphology and chemical/electronic structure were characterized using various complementary methods, including X-ray diffraction, electron microscopy, X-ray photoelectron spectroscopy and scanning transmission X-ray microscopy. The presence of both reductive and oxidative surface states was evidenced and their impact on the photoelectrochemical efficiency was characterized. We show that both electronic conduction enhancement provided by the Ti substitution and charge transfer promoted by oxidative surface states improve the solar water splitting performance.

Introduction

In the framework of research on clean, secure and efficient energy, hydrogen production by solar water splitting (SWS) is a very promising method. In this process, sunlight is used to reduce the voltage bias necessary to split hydrogen directly from a water molecule, an idea inspired by the photosynthesis in plants. The first report on SWS (in the early 70s) used n-type TiO_2 as a model photoanode.[1] Due to its wide band-gap (3.2 eV) n-type TiO_2 can absorb only ultraviolet (UV) radiation which corresponds to just 4% of the solar energy reaching the Earth's surface.[2] Since then, research on many semiconducting materials has identified lower band-gap materials that absorb light in the visible range, such as Fe_2O_3,[3,4] WO_3,[5,6] $BiVO_4$,[6,7] $BaTiO_3$,[8] *etc.* As reported by Chen *et al.* in 2010,[9] the theoretical values for the photocurrent and solar-to-hydrogen efficiencies decrease when the band gap increases. For α-Fe_2O_3, $BiVO_4$, WO_3 and $BaTiO_3$ theoretical photocurrents of 12.6 mA cm^{-2}, 7.5 mA cm^{-2}, 6 mA cm^{-2} and 1.2 mA cm^{-2} were predicted, respectively. Hematite (α-Fe_2O_3) is a semiconducting iron oxide with a band gap of 2.15 eV allowing it to absorb 40% of the solar spectrum bandwidth, which is quasi optimal for direct SWS applications.[4,10,11] Compared to materials exhibiting higher photocurrents,[6] hematite appears to be less efficient for SWS because of a reduced mean free path (~2–4 nm) of holes[10] and poor kinetics during the oxidation evolution reaction at the hematite/electrolyte interface.[12,13] Nevertheless, hematite is vastly abundant, not expensive and environment friendly, assets that need to be considered. Two axes emerged in research to improve hematite-based SWS systems. First, model continuous and homogeneous hematite thin films with controlled crystallography, electronic structure and stoichiometry were obtained using in-vacuum evaporation techniques like atomic oxygen assisted molecular beam epitaxy,[4,8,14] magnetron sputtering,[13] pulsed-laser-deposition,[15] or atomic layer deposition.[16] Such samples allow studies of the photoelectrochemical (PEC) efficiency by varying each parameter (*i.e.* thickness, chemical composition, crystallographic structure, *etc.*) independently. Second, nanostructuring hematite was found to be one solution to drastically improve the PEC efficiency by increasing the number of photo-charges collected during SWS, mainly through fine control of the morphology. Therefore, considerable effort was dedicated to obtain as-grown nanostructured/self-assembled films of hematite (nano-wires or nano-rods, column-like porous architectures, core–shell structures, *etc.*). Various methods were reported in the literature: aqueous chemical growth (ACG),[17,18] spin-coating,[7] electrodeposition,[19,20]

[a]Service de Physique de l'Etat Condensé (SPEC), CEA, CNRS UMR 3680, Université Paris-Saclay, Orme des Merisiers, CEA Saclay, 91191 Gif-sur-Yvette Cedex, France. E-mail: dana.stanescu@cea.fr

[b]Synchrotron SOLEIL, L'Orme des Merisiers, Saint-Aubin, BP 48, 91192 Gif-sur-Yvette Cedex, France. E-mail: stefan.stanescu@synchrotron-soleil.fr

[c]Institut de Physique et Chimie des Matériaux de Strasbourg (IPCMS), UMR 7504 CNRS – Université de Strasbourg, 23 rue du Loess, BP 43, Strasbourg Cedex 2, France

[d]Nanosciences et Innovation pour les Matériaux, la Biomédecine et l'Énergie (NIMBE), CEA, CNRS UMR 3685, Université Paris-Saclay, CEA Saclay, 91191 Gif-sur-Yvette Cedex, France

[e]Sorbonne Universités, UPMC Univ. Paris 06, CNRS, Laboratoire de Chimie Physique – Matière et Rayonnement (UMR 7614), 4 place Jussieu, 75252 Paris Cedex 05, France

[f]Chemistry & Chemical Biology, McMaster University Hamilton, ON, Canada

† Electronic supplementary information (ESI) available: Table SI-1 and Fig. SI-1–SI-11. See DOI: 10.1039/d0ta06524b

sol–gel,[21] *etc.* The resulting photoanodes are not homogeneous in terms of morphology, crystallography, or electronic or chemical structure, such that many different surface states might coexist on the same hematite photoanode. Irrespective of the synthetic method, the oxygen evolution reaction (OER) at the hematite/electrolyte interface during SWS occurs as an indirect process and the kinetics are low. Thus, a large external potential is required to drive the oxidation. The holes are first trapped by surface states[22,23] favoring the formation of Fe–O or Fe–OH, which, in the second step, dissociate water molecules in a charge transfer process. The surface kinetics depends on the efficiencies of both electron–hole surface recombination and charge transfer.[22] It has been shown that Ti-doped hematite[24] or Co-based[25] or Co-phosphate (Co-Pi)[26] coating layers on hematite reduce the surface recombination rate. In contrast, when the coating layer is Al_2O_3 (ref. 27) a passivation effect of the overlayer on the surface states can be observed which leads to a direct transfer of the holes to the electrolyte. Unfortunately, the Al_2O_3 coating was not stable and dissolved after 1 hour of operation.

Global PEC performance of photoanodes in a photoelectrolysis reaction depends on a multitude of parameters like carrier conductivity, surface kinetics, light absorption, photovoltage, onset potential, *etc.* Electric conduction can be improved by doping hematite with Ti as shown in previous studies.[4,25] Surface kinetics during SWS is strongly related to surface states at the photoanode/electrolyte interface. These have various origins such as oxygen vacancies on the as-grown hematite[28] or highly oxidized Fe species.[29] Surface states play an important role in the PEC efficiency by governing charge transfer between the photoanode and the electrolyte in an indirect or direct transfer process. UV-visible light absorption is quasi-optimal for hematite based photoanodes.[4,10,11] The photovoltage induced by light absorption shifts the onset potential for SWS to lower values. For hematite in contact with an electrolyte the photovoltage value is limited by the potential drop in the Helmholtz layer at the hematite/electrolyte interface.[30] For a complete understanding of the SWS reaction, we must weigh the effect of each of these processes on the total PEC performance and optimize the most significant ones. Understanding the OER mechanism, the miscellaneous origins of surface states – resulting in both beneficial and detrimental impacts on the reaction efficiency – is the key for increasing the efficiency of the hematite photoanode.[31]

Here we report the results of a comprehensive study aiming at understanding the nature and origin of the surface states and their role in the PEC performance of hematite photoanodes prepared by ACG. For this purpose, we compared hematite and Ti substituted hematite samples, varying the annealing temperature from 500 °C to 600 °C. We disentangled electronic conduction enhancement from surface state effects upon Ti substitution by using a multiscale approach with a wide range of macro and microscopic techniques in order to tackle the inherent complexity of this system. To obtain a complete insight into the PEC activity, we performed exhaustive quantitative characterization: fast-sweep voltammetry, incident photon-to-current efficiency spectroscopy, electrochemical impedance spectroscopy, and open-circuit measurements for flat-band and onset potential characterization. The crystallographic structure was determined by *in situ* X-ray diffraction experiments during the phase transformation from the intermediate akaganeite to the final hematite. Finally, the chemical and electronic structures at the nanoscale were determined using synchrotron X-ray spectro-microscopy and are discussed in correlation with the PEC and crystallographic results. The combination of these results provides evidence for the existence of antagonist surface states (with reduced or oxidized character) driven by the intrinsic morphology and microstructure of ACG synthesized hematite photoanodes.

Experimental section – methods

Aqueous chemical growth of pure and Ti-substituted hematite photoanodes

Pure and Ti-substituted Fe_2O_3 photoanodes were grown on F:SnO_2 (FTO) substrates by a two-steps process. First, akaganeite (β-FeOOH) films were prepared by ACG, using an approach similar to that presented by Vayssieres *et al.*[17] Second, the akaganeite phase was converted to hematite by air-annealing. The method used to clean the FTO substrates, commonly used for solar insolation related applications, was crucial to produce homogeneous photoanode films. The cleaning protocol which allowed perfect reproducibility of the ACG grown akaganeite films consisted of three steps. First, the FTO substrates were cleaned by ultrasonication in an acetone (VLSI Selectipur, purity > 99.5%) bath for 15 min, and then they were rinsed in isopropanol (VLSI Selectipur, purity > 99.5%) and distilled water followed by nitrogen drying and annealing at 110 °C in air on a hot plate for another 15 min. Second, impurities (mainly carbon) were removed by 5 min oxygen plasma treatment (100 W/0.2 mbar). Third, 2 min of UV irradiation (50 mW cm^{-2}) followed by a distilled water rinse was used to render the FTO surface hydrophilic. For the deposition process, we used as-received $FeCl_3$ (anhydrous iron(III) chloride, 98% from Fisher Scientific) and $TiCl_3$ (20% w/w sol from Fisher Scientific) precursors that were dissolved in Millipore grade water to obtain aqueous solutions. The cleaned substrates were then dipped in these solutions in closed bottles. Hydrothermal activation of the deposition was achieved by maintaining the bottles at 95 °C for several hours in an oven. At the end of the deposition process, the samples were rinsed in three baths of distilled water, assisted by low power ultrasonication for one minute. The akaganeite film morphology can be controlled by varying the pH value of the aqueous solution, the deposition time and the substrate position (height and inclination angle) in the bottle. For this study, the pH of the growth solution (1.4) and the temperature during the growth (95 °C) were the same for all the samples. These growth parameters produce films with a carpet-like morphology, with akaganeite nanorods oriented perpendicularly to the FTO substrate. Hematite was obtained by air-annealing at 500 °C and 600 °C. Ti doping was obtained by adding a 0.3 wt% $TiCl_3$ (20% w/v in 2 N HCl) precursor in an $FeCl_3$ aqueous solution with pH = 1.4. It is known that the deposition rate for Ti-substituted hematite is lower than that for pure hematite.[32] Indeed, Ti

inhibits the akaganeite nanorod growth and consequently decreases the average hematite equivalent thickness, as discussed later in this paper. Therefore, in order to produce comparable samples, all with a film thickness of ~200 nm, the deposition time was adjusted accordingly. Four samples, from S1 to S4, were prepared and investigated here. S1 and S2 correspond to pure-hematite samples, air-annealed at 500 °C (S1) and 600 °C (S2). S3 and S4 are Ti-substituted hematite samples air-annealed at 500 °C (S3) and 600 °C (S4). Details can be found in ESI Table SI-1.†

Scanning electron microscopy

Morphology plays an important role in the resulting PEC properties as already reported in the literature[14,18,33,34] and confirmed in this study as well. Extensive scanning electron microscopy (SEM) was thus employed at three different stages of the study. First, before the annealing when the akaganeite phase is obtained from the hydrothermal growth. At this stage, the carpet-like morphology is already formed and SEM was used to qualify the samples for the next annealing step. Second, after the annealing, the final hematite phase was characterized and, in particular, the homogeneity of the sample was checked. Third, SEM was used to identify the regions of interest (ROI) to be measured afterwards using synchrotron spectromicroscopy. All SEM measurements were performed on Zeiss SEM-FEG Supra55VP apparatus hosted at the CNRS IPANEMA laboratory, allowing fast measurements through easy and precise tuning of the microscope parameters. Two different sets of parameters were used, measuring in each case the secondary electrons: first, the topography was characterized using low acceleration potential values, between 1.5 and 3 kV, with an Everhart Thornley (SE2) detector. Second, high acceleration potential values, between 10 and 15 kV, with an InLens (SE1) detector, allowed increased resolution and higher electron penetration, which were used to characterize the samples prior to the scanning transmission X-ray microscopy (STXM) measurements.

X-ray diffraction

Synchrotron *in situ* X-ray diffraction (XRD) measurements were performed at the DiffAbs beamline at the Synchrotron SOLEIL facility. The beamline is equipped with a 6-circle diffractometer (kappa geometry), allowing for precise sample positioning and angular orientation in order to perform experiments in different geometries (specular, coplanar and/or grazing incidence) and the use of variable temperature sample environments for studying *in situ* sample transformation. The scattering experiments reported hereafter were performed at photon energies of 15 keV (0.82 Å wavelength). The reported data are given in momentum transfer q coordinates. The X-ray photon beam was monochromatized using a Si (111) double crystal monochromator ($\Delta E/E \sim 10^{-4}$) and focused horizontally and vertically. The result is a spot size at the sample position of about 250 × 250 μm^2 FWHM, a beam divergence ~ 0.01° × 0.1° (vertical × horizontal), and a photon flux of 10^{12} ph per s. The diffraction data were recorded using a hybrid pixel area detector (XPAD-S140) consisting of a matrix of 240 × 560 pixels with a pixel size of 130 μm.[35–39] The detector has no dead areas and is mounted at a distance of 400–700 mm from the sample (depending on the type of the experiment performed), with its long dimension along the vertical direction (angular opening in the 2θ direction of 6° to 10°). The low noise and low background, large dynamic range (over almost 6 decades) and good sensitivity make it an optimal device to measure powder XRD signals over an extended angular range in a single acquisition. The procedure to convert the XPAD images into intensity *vs.* 2θ diffractograms is described in ref. 38 and 39. For the air *in situ* annealing experiments a heating plate (Anton Paar DHS 900 model) was used, with a PEEK (poly-ether-ether-ketone) dome. The air-annealing was performed using a ramp of 4 °C min^{-1}, and diffraction data (XPAD images of 10 s of exposure each) were acquired every 30 s. The measurements are performed using fixed sample incidence (9.25°) geometry. In order to reduce the parasitic scattering (dome or substrate), the sample consisted of a half covered substrate. Subsequent acquisitions of regions corresponding to the akaganeite/hematite layer and bare substrate respectively are performed, and they are then subtracted, which results in an improvement of the XRD layer signal (but does not necessarily totally remove the parasitic signal, due to possible sample misalignment or drift). The results reported in this paper correspond, most of the time, to the corrected data; the "parasitic signal" regions, which are not always perfectly corrected, are sometimes masked/shaded.

Photoelectrochemical activity: setup and protocol

We want to emphasize in this section the importance of the methodology used to measure PEC activity of the photoanodes, since many reports in the literature simply give photocurrent values which are implied to be the ultimate parameter relating to the SWS efficiency of the material. In our view, it is only by considering all of the PEC parameters, recorded as described here, that artifact-free characterization and a valid comparison can be achieved. The PEC activity of the hematite-based photoanodes was characterized by five types of measurements: (i) fast sweep voltammetry, (ii) time stabilized photocurrent measurements, (iii) incident photon-to-current efficiency (IPCE) spectroscopy, (iv) open-circuit voltage measurements and (v) electrochemical impedance spectroscopy (EIS). For this purpose, we used a dedicated setup equipped with an UV-vis light source (Newport 1000 W Xe arc lamp), a Cornerstone 130 model 74004 monochromator (Newport), a three-electrode cell,[4] a Princeton Applied Research 263A potentiostat and a PAR 5210 lock-in amplifier. All measurements were performed at room temperature (RT) using 0.1 M NaOH as the electrolyte in the three-electrode cell where the samples are the working electrode, a platinum wire is the counter electrode, and Ag/AgCl is the reference electrode.

Fast sweep voltammetry. During fast sweep voltammetry measurements, a potentiostat is used both to vary the applied potential (V) between the working and the reference electrode and to measure the resulting current density (J) flowing in the counter electrode. The potential was swept with a rate of 50 mV

s^{-1}. Current measurements were performed in the presence and the absence of light (ON and OFF, respectively), the photocurrent density (J_{ph} – red curves in Fig. SI-1b and d†) being defined as the difference between the current density recorded with light (J_{ON}) and without light (J_{OFF}):

$$J_{ph} = J_{ON} - J_{OFF} \quad (1)$$

The electrochemical reactions are usually slow with characteristic times in the range of milliseconds to seconds.[40] Slow dynamic processes like diffusion near the electrodes, molecule trapping on the surface states during the reaction, and stray capacitances may affect the photocurrent value and the reproducibility of the measurements.[41] For this reason, the sweep rate used in this case was fast, such that the system did not have enough time to stabilize at each applied potential. Transient signals followed by a stabilization process occur for each variation of the potential but also when the light is switched between ON and OFF for a constant potential as shown in Fig. SI-1a and c.† The blue curves presented in Fig. SI-1b and d† are obtained by switching the light ON–OFF using a mechanical shutter every 1 second during fast sweep voltammetry measurements. The transients recorded by these measurements are related directly to the surface recombination phenomena involving surface states at the photoanode–electrolyte interface.[42] Increasing (or decreasing) the sweep rate of the applied voltage will increase (or, respectively, decrease) the measured photocurrent for the same sample. Therefore, for samples presenting large transients, the photocurrent measured by fast sweep voltammetry is over-estimated.

Time stabilized current density measurements. In order to measure a pertinent photocurrent value, independent of the experimental parameters used, for instance the sweep rate described above, we performed time stabilized measurements in a double stabilization scheme, as follows. The current density is measured at a constant voltage (V) as a function of the time (Fig. SI-1a and c†). Stabilization typically takes several minutes, the time necessary to reach an asymptotic regime. Initially the shutter is closed and J_{OFF} is measured. When the dark current is stabilized the shutter is opened. A step change preceded by a transient signal is observed. In the same manner, we wait to reach stabilization under light (J_{ON}). Therefore, the stabilized photocurrent at the voltage V corresponds to the step height after stabilization ($J_{ON} - J_{OFF}$) as shown in Fig. SI-1a and c.† We perform the same experiments for several voltages and then we represent the stabilized photocurrent as a function of the voltage, $J_{stab}(V)$ (red dots in Fig. SI-1b and d†). If the transients are very important like for sample S1 (Fig. SI-1a†) the stabilized photocurrent is lower than the one measured during a fast-sweep (the values corresponding to the red dots are lower than the ones corresponding to the red curve in Fig. SI-1b†). No transients are observed for sample S4 during the ON–OFF voltammetry (Fig. SI-1d,† blue curve); therefore stabilized photocurrent values (red dots in Fig. SI-1d†) are the same as the fast-sweep photocurrent (red curve in Fig. SI-1d†).

IPCE spectroscopy. Incident photon-to-current efficiency spectroscopy – IPCE(λ) – measurements were realized by measuring the photocurrent density as a function of the incident light wavelength, $J_{ph}(\lambda)$, while keeping the applied potential constant. The measurement starts after a stabilization time of 200 s. A LabView® control interface was designed for IPCE measurements tuning the monochromator and the potentiostat, while Python scripts were developed for data treatment. The IPCE values were calculated using the formula:

$$\mathrm{IPCE}(\lambda) = \frac{N_{elec}}{N_{ph}} = \frac{hc}{\lambda} \times \frac{J_{ph}(\lambda)}{eP(\lambda)}\,(\%) \quad (2)$$

where N_{elec} is the number of photoelectrons, N_{ph} is the number of photons, h is the Planck constant, c is the speed of light in a vacuum, λ is the light wavelength, $J_{ph}(\lambda)$ is the photocurrent density, e is the electron charge and $P(\lambda)$ is the incident light flux measured with a Newport 1918-R power meter.

The lamp power was calibrated prior to each measurement in order to minimize errors originating from variations from one experiment to another due to lamp ageing, changing monochromator alignment, *etc.* Integrated lamp power values normalized with respect to 1 Sun for each sample are presented in Fig. SI-2† showing variations from around 0.4 to 0.6. The photocurrent values reported in this paper are all extrapolated to 1 Sun assuming a linear dependence of the photocurrent on the UV-vis light power.

Open-circuit voltage measurements: photovoltage and onset potential. Photovoltage measurements were performed by recording the open-circuit potentials in the dark (V_{OFF}^{OC}) and under light (V_{ON}^{OC}). For this purpose, we measured the potential of the working electrode (our sample) by keeping the current in the counter electrode zero. For each measurement, we wait several minutes to reach an equilibrium and to record a stable value of the potential. In the dark, the equilibrium potentials should be equal to 1.23 V. Because of the potential drop in the Helmholtz layer at the interface between the photoanode and the electrolyte this value is lower, 0.85 V.[30] Under light, the equilibrium between the photoanode and the electrolyte is reached at a potential corresponding to the quasi-Fermi level of the holes. V_{ON}^{OC} is equal to the onset potential,[25] *i.e.* the minimum potential at which photoelectrolysis occurs, and the photovoltage can be calculated as:

$$V_{ph} = V_{OFF}^{OC} - V_{ON}^{OC} \quad (3)$$

Electrochemical impedance spectroscopy (EIS) measurements. Electrochemical impedances were measured for several DC biases (V_0) between 0.4 and 1.6 V *vs.* RHE by superimposing a sinusoidal potential, $V(\omega)$, of 10 mV RMS amplitude, with frequencies varying between 10 Hz and 100 kHz. A potentiostat connected to a lock-in amplifier was used to apply the potential, $V = V_0 + V(\omega)$, between the working electrode (the sample) and the reference electrode and to measure the AC currents obtained in the counter electrode, $I(\omega)$. The complex impedance, which is defined as:

$$Z = \frac{V(\omega)}{I(\omega)} = Z' + \mathrm{j}Z'' \quad (4)$$

contains information on the RC-like equivalent circuit corresponding to the photoanode–electrolyte interface. In this work, we approximated the equivalent circuit as a resistance R_0 in series with a $R_{SC}C_{SC}$ circuit corresponding to the semiconductor (SC) oxide and in series with a R_HC_H circuit corresponding to the Helmholtz double layer at the SC/electrolyte interface (inset in Fig. SI-3†).

As shown by Mei *et al.*,[43] several parameters can be deduced from Nyquist plots, $Z'' = f(Z', f)$, including resistance (of the electrodes, of the electrolyte, and of the diffuse layer) and capacitance values. Additionally, the slope of the Nyquist plot at intermediate frequencies (Fig. SI-3†) is a measure of the extent of ion diffusion through the Helmholtz layer, which occurs after the double layer formation. Modeling of EIS data obtained from imperfect dielectrics (like our oxide semiconducting sample in this case) is usually realized by replacing ideal capacitors with constant phase elements (CPEs). The impedance of a CPE can be calculated using:

$$Z_{CPE} = \frac{1}{(j\omega)^n Q_0} \quad (5)$$

where Q_0 and n are frequency independent constants at a given temperature and n can take values between 0 and 1, with $n = 1$ for an ideal capacitor.

EIS data obtained for several applied voltages were fitted using Python scripts. This allowed determination of the values of all the parameters of the equivalent circuit model. Moreover, flat band values can be determined from the Mott–Schottky plots $1/{C_{eff}}^2 = f(V_0)$ where:

$$C_{eff} = {\omega_{max}}^{n-1} \times Q_0 \quad (6)$$

and ω_{max} corresponds to the frequency at which the imaginary part of the impedance (Z'') has a maximum.[44] This formula, which was developed by Hsu and Mansfeld[44] and is similar to those reported by Brug *et al.*[45] and Hirschorn *et al.*,[46–48] models interfacial capacitances as normal or surface distributions of time constants.

Deformations of the shape of Mott–Schottky plots and, consequently, variations of the flat band values, are directly related to the presence and nature of surface states at the electrode–electrolyte interface which induce Fermi level pinning[49,50] while varying the voltage. This aspect is analyzed and discussed in more detail in the results section.

X-ray photoemission spectroscopy

X-ray Photoemission Spectroscopy (XPS) was first used to check the chemical and the electronic structure of hematite nanorods. Measurements were carried out using a Kratos Axis Ultra DLD spectrometer with a monochromatic Al K_α (1486.6 eV) X-ray source and a charge compensation system. Spectra were collected at an analyzer pass energy of 40 eV for individual core level spectra. The binding energy scale was calibrated using the position of the adventitious C 1s line at 285 eV. While XPS allows a rapid overview of the samples, it is not well adapted to these kinds of samples since it only probes the outermost surface of the nanorods. The mean free path of photoelectrons with a kinetic energy of 700 eV is around 1 nm (ref. 51) and the XPS intensity decreases exponentially with increasing depth. The maximum generally admitted probing depth (yielding more than 95% of the XPS signal) is $3 \times \lambda_e \times \cos(\theta_e)$, where λ_e is the electron mean free path at a given kinetic energy and θ_e is the electron escape angle with respect to the surface normal. Thus, we can assume that the XPS signal does not probe regions deeper than 3 nm inside the photoanode films.

Scanning transmission X-ray microscopy

Scanning transmission X-ray microscopy (STXM)[52] is well adapted to probe the morphology and chemistry of these samples due to the large penetration of X-rays and to the strong chemical sensitivity of X-ray absorption spectroscopy (XAS).[53] STXM was performed at the HERMES beamline of the Synchrotron SOLEIL.[54] The transmission geometry ensures probing the bulk properties of the hematite nanorods and the soft X-ray regime (100–1000 eV) offers strong chemical coordination sensitivity since it probes unoccupied electronic states in the band gap and the conduction band of hematite. A full picture of the electronic structure was accessed by tuning the X-ray energy across the Ti and Fe $L_{2,3}$ and O K absorption edges. The spatial resolution allows STXM to map the chemical heterogeneity, in particular that of the Ti substitution. A STXM image is obtained in raster mode, point by point. The transmitted intensity at each pixel follows the Beer–Lambert absorption law:

$$I_t = I_0 \times e^{-\mu(E)\times\rho\times t} \quad (7)$$

where the measured transmitted intensity (I_t) is related to the incident X-ray intensity (I_0), sample thickness (t), density (ρ) and energy dependent linear absorption coefficient (μ). The sample is scanned through the focal spot of the X-ray beam using interferometrically controlled positioning. A Fresnel Zone Plate (FZP) is used to focus the X-ray beam and its first diffraction order is filtered using an order sorting aperture (OSA) in combination with a central stop on the FZP. For these experiments, we used an FZP with a 35 nm outer zone width, giving a theoretical spot size of around 43 nm. In practice, the achieved experimental resolution is limited by beam, sample and detection instabilities and drifts. In particular in the case of acquisition over long spectral ranges, as used in this case, the spectral information is smeared over a few pixels. Thus, the resolution during these experiments was ~60 nm. The central stop of 80 μm defined on the FZP and the 50 μm OSA ensured the use of only the first diffraction order. All STXM measurements were performed using a broad energy range from 450 to 850 eV, covering the Ti $L_{2,3}$, O K and Fe $L_{2,3}$ edges. Full 3D datasets $I(x,y,E)$ were obtained by recording STXM images at each energy point. The data were treated (*e.g.* drift correction), converted to optical density (OD) and analyzed using aXis2000 (http://unicorn.mcmaster.ca/aXis2000.html), MANTIS (http://spectromicroscopy.com), ImageJ (https://fiji.sc) and Python (https://www.python.org).

The as-deposited samples could not be used directly for the transmission measurements since the FTO/glass substrate is

too thick for the given energy range. Two different approaches were employed to prepare the samples for STXM measurements. First, the scratched surface of the sample was wiped with a standard transmission electron microscopy (TEM) 3 mm copper grid. In this way, chunks of the nanostructured hematite films were transferred from the FTO samples to the Cu grid, achieving measurable portions with a sufficiently high probability. Second, sub-100 nm slices were produced by ultramicrotomy (UMT). The advantage of the second approach is that it preserves the interface region between the FTO and the hematite film. Nevertheless, UMT is very time-consuming, in particular for this kind of sample deposited on glass, requiring laborious preparation. Indeed, in order to produce useful samples, a special protocol was developed. The 1.1 mm glass substrate was first thinned in pure hydrofluoric acid (HF) until a thickness of a few micrometers was obtained, ensuring retention of the hematite/FTO interface upon slicing. For this reason, very few selected samples were cut by UMT.

Results and discussion

Morphology

Hematite grows in the expected carpet-like morphology, *i.e.* with the hematite nanorods grown perpendicular to the FTO-coated glass substrate. Fig. 1a presents a typical SEM image of the hematite phase on the FTO substrate for the S1 sample. All samples studied present a similar morphology, *i.e.* the 1 × 1 cm^2 sample area is uniformly covered by nanorods perpendicular to the substrate. The morphology of hematite nanorods grown by ACG has been described previously in the literature.[55–57] It is important to stress here that the morphology of the hematite nanorods strongly depends on the growth conditions, including the deposition time, doping and annealing temperature. The influence of annealing temperature on the nanorod morphology is clearly demonstrated in the SEM images of the UMT cuts from the samples S1 (Fig. 1b) and S2 (Fig. 1c).

Indeed, the length of the pure hematite nanorods decreases by 30% when the annealing temperature is increased from 500 °C to 600 °C. This effect is less obvious for the Ti substituted samples, where the annealing temperature doesn't seem to strongly affect the nanorod length. But Ti substitution strongly inhibits the hematite nanorod growth, with a further decrease of at least 50% in length with respect to pure hematite, visible when comparing Fig. 1c and d and also clearly shown in the graph in Fig. 1e. We tested several Ti aqueous solution concentrations from 0.06 to 0.6 Ti wt% (results not presented here). For the highest Ti content the nanorod growth is fully suppressed. In Fig. 1e we report the measurements of the nanorod lengths obtained from all the samples grown during 24 hours. For the sake of comparison of the PEC activity between all the samples we choose to vary the growth times as shown in Table SI-1.† In this manner samples were fabricated with

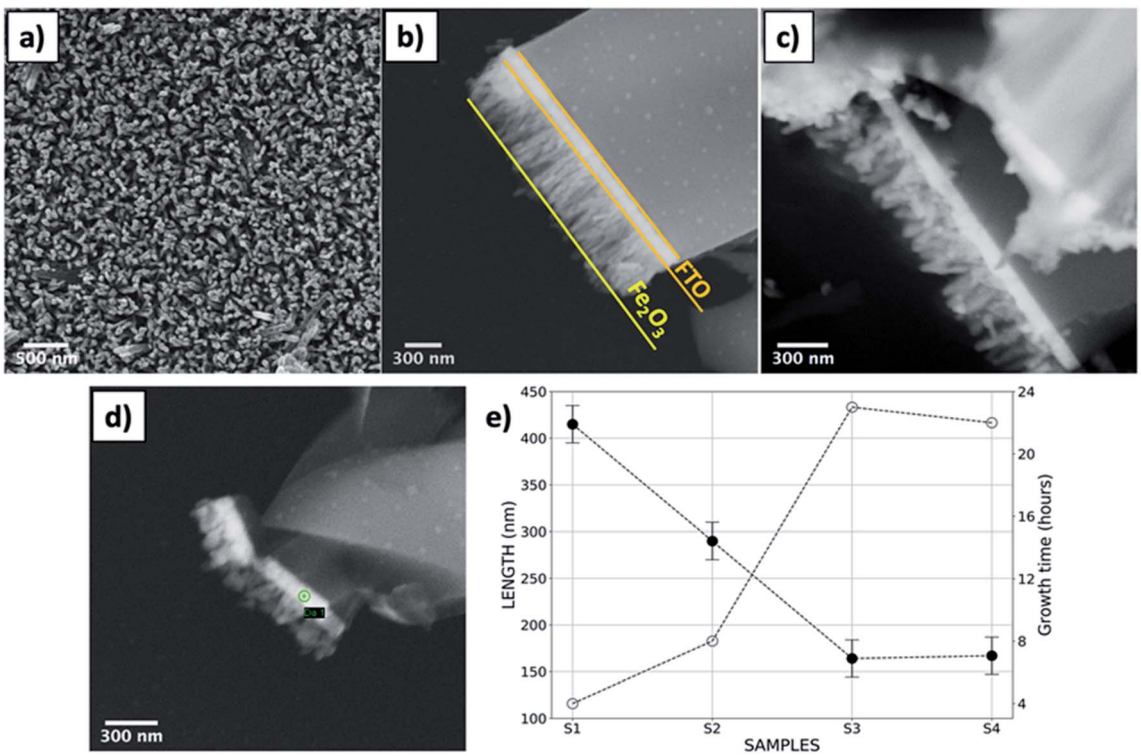

Fig. 1 SEM images for the S1 ((a) as-deposited and (b) UMT cut sample), S2 (c) and S4 (d) 24 hour deposited samples. The FTO and hematite regions are clearly distinguished as shown in (b). All SEM images were obtained with an acceleration potential of 15 kV and using an InLens detector. Images from the UMT cut samples were rotated so that the nanorods point in the same direction to facilitate visual comparison; (e) nanorod length (●) for the 24 hour deposited samples and the growth time (○) needed to obtain similar lengths of the hematite nanorods.

similar lengths for the Ti substituted and pure hematite nanorods, *i.e.* ~200 nm.

Crystallographic structure

In situ annealing XRD experiments were performed for the pure and the Ti substituted samples. By combining all the diffractograms obtained during the annealing, color maps highlighting the evolution and the structural phase transformation are obtained (Fig. 2a and b). The (121) diffraction peak of the akaganeite phase at $q \sim 24.8\ \mathrm{nm}^{-1}$ starts to significantly move toward larger q values for temperatures $T \in [180\ ^\circ\mathrm{C}–200\ ^\circ\mathrm{C}]$ and diminishes in intensity, before (almost) vanishing at $T \sim 300\ ^\circ\mathrm{C}$. Concomitantly, we observe the formation of the hematite (110) peak at a slightly larger q value, $25\ \mathrm{nm}^{-1}$, indicating a contraction of the inter-reticular distance along the nanorod direction, *i.e.* perpendicular to the sample surface. More details can be extracted if the corresponding diffraction profile is modeled (using, in this case, a Gaussian profile). The area of the XRD peak (integrated intensity) is proportional to the amount of the crystalline phase. Its position can be used to extract the corresponding inter-reticular distance, d. The full width at half maximum (FWHM) of the peak contains several components, including the size of the constituent crystallites and micro-strain. By measuring several orders of diffraction peaks, it is possible to extract the individual contributions (considering that their contribution *vs.* momentum transfer q is different). In the following, we assumed that the effect of the micro-strain is negligible, and the peak width is essentially given by the size of the constituent crystallites. Thus, crystallite size is reported using the Scherrer formula:

$$\mathrm{Size} = \frac{K \times \lambda}{\Delta(2\theta) \times \cos\theta} \tag{8}$$

where the shape factor $K = 1$, λ is the X-ray wavelength, θ is the Bragg angle, and $\Delta(2\theta)$ is the FWHM after correcting for instrumental resolution, which is about 0.02°. The results for the pure and Ti substituted samples are reported in Fig. 2c–e using filled blue and red dots, respectively. It should be noted here that in the case of the Ti substituted sample, the scattered intensity for T higher than ~330 °C becomes extremely low and is no longer visible in the colored maps (Fig. 2b). Although the automatic fit procedure seems to detect the peaks, the results are rather spread out – this is the reason why they are represented using a red dotted line. Even so, trends are still visible. Based on the fitted data for the pure sample, several temperature regimes can be identified, as indicated by alternating color regions in Fig. 2c–e:

(i) Chlorine loss, $T \in$ [RT, 200 °C]: the XRD peak intensity (Fig. 2c) diminishes slightly (by ~20%) with increasing temperature. In the same regime, the corresponding inter-planar distance (Fig. 2d) is slightly contracted (by ~0.4%). The crystallite size diminishes to about 20 nm which is somehow counter-intuitive since thermal expansion was expected. Such behavior was not observed by Gualtieri and Venturelli[58] who studied the transformation of goethite (α-FeOOH) into hematite. There are two main differences compared to the above cited study that need to be considered for a direct comparison of the main observations: first, in our case, the measurement is performed not on a polycrystalline powder but on a carpet of akaganeite needles, oriented perpendicular to the sample surface, with the majority aligned along the [121] direction. Therefore, our measurement is very sensitive to this particular direction. Second, even though both are iron oxyhydroxides and therefore subject to water loss upon annealing, in contrast to goethite, akaganeite contains chlorine in its structure. Thus, it appears that in this temperature range some of the Cl is

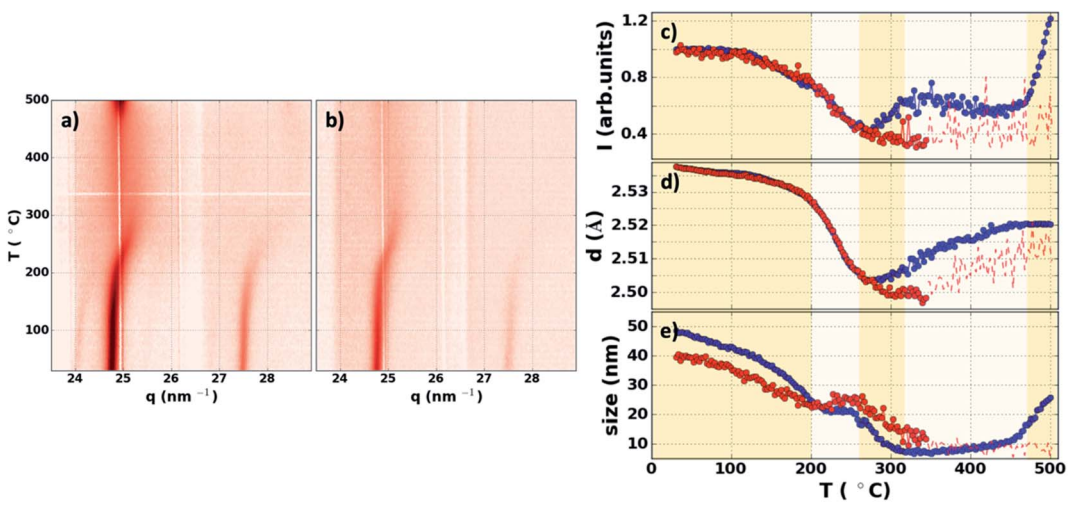

Fig. 2 XRD data represented as a color-map as a function of the momentum transfer q and temperature during the *in situ* annealing. The same logarithmic color scale is used in both cases for the pure (a) and Ti substituted (b) samples, from white to red, and spans over about 1 decade. The XRD peak at $q \sim 24.8\ \mathrm{nm}^{-1}$ corresponding to the (121) reflection in akaganeite and (110) in hematite, is fitted using a Gaussian function, and the results (integrated intensity, corresponding inter-reticular distance and deduced crystallites size) are reported, as a function of the annealing temperature, in panels (c)–(e). Blue and red symbols are, respectively, used for pure and Ti substituted samples. Several temperature regimes defined relative to the pure sample are highlighted by the shaded areas and are discussed in the text.

removed from the akaganeite structure resulting in a decrease of the reticular distance. It is interesting to note that, at RT, the average crystallite size in the Ti substituted sample (Fig. 2e) is reduced by ~20% as compared to that in the pure hematite one, explaining and supporting the SEM results showing the reduction of the nanorod length upon Ti incorporation. Remarkably, at 200 °C both samples show a similar crystallite size (~20 nm). This similarity may suggest the existence of two kinds of Ti in the structure: one type of Ti substitutes Fe inside the Fe–O_6 octahedra; the second type is bonded with the Cl from the "tunnel" akaganeite structure.[59,60] Thus, the Cl directly bonded to Ti is stabilized and less volatile with increasing temperature. Indeed, a slowdown behavior can be observed on all extracted XRD parameters in the higher temperature regime for the Ti substituted sample.

(ii) Hydroxyl loss, $T \in [200\ °C, 260\ °C]$: in this temperature regime the XRD peak intensity diminishes to ~40% of its initial value at RT. The corresponding inter-planar distance also contracts by more than 1%, while the crystallite size seems to maintain its value in the ~20 nm plateau. This temperature regime seems to highlight the rapid consumption of the akaganeite crystalline phase. Interestingly, this temperature range is in perfect agreement with the goethite transformation reported in ref. 58 which was attributed to rapid water/OH loss. The constant crystallite size in concert with the decrease of the diffraction intensity suggests that the value of ~20 nm is the minimum thermodynamically stable akaganeite crystallite size, with further OH loss resulting in vanishing of the akaganeite long-range structure.

(iii) "Protohematite"[58] germination, $T \in [260\ °C, 315\ °C]$: in this regime, the XRD peak intensity and inter-reticular distance start to increase, while the corresponding crystallite size drops to ~7 nm. The increase of the diffraction intensity is associated with an evident re-crystallization process, resulting in the appearance of new crystalline germs, most probably the proposed disordered "protohematite",[58] a non-stoichiometric intermediate phase, characterized by Fe vacancies and consequently by excess of OH for charge balance (each missing Fe^{3+} cation is replaced by three protons). The Ti substituted sample exhibits a ~50 °C "delay" in this region compared to the pure one; the diffraction intensity and the inter-reticular distance reach their minima only toward ~315 °C.

(iv) Structure stabilization, $T \in [315\ °C, 475\ °C]$: this broad temperature range is characterized by invariability of the tracked XRD parameters, in particular the peak intensity and the crystallite size, while the inter-reticular distance continues its slow increase. It seems to be related to a stabilization process, driven by the healing of Fe-defective "protohematite", by a slow and continuous OH loss and consequently by filling the Fe vacancies, similar to the *in situ* observations during hydrothermal growth of the same system by Peterson *et al.*[60] It is difficult to discuss the Ti substituted sample since the diffraction intensity is very low. Nevertheless there is a visible trend which follows that of the pure hematite sample, again with a ~50 °C "delay".

(v) Oriented aggregation, $T \in [475\ °C, 500\ °C]$: in this regime the intensity of the XRD peak sharply increases, reaching values larger than the ones measured for the as-prepared sample and indicating an increased crystallized volume. At the same time, the crystallites rapidly grow reaching average sizes of ~25 nm, while the inter-reticular distance seems to have reached a constant value of 2.52 Å. This temperature range corresponds to the growth of the ordered hematite phase, as proposed in ref. 58. More recent studies[61–63] provide evidence of a multistep oriented aggregation mechanism that seems to occur for various hydrothermally grown iron oxides and oxyhydroxide (hematite, magnetite, and ferrihydrite) crystals and that is fully coherent with our observations. The final hematite crystal results from the aggregation of multiple mesocrystals (originating from the incipient akaganeite), explaining both the increase of the crystal size and of the overall diffracting volume close to 500 °C. Due to the *in situ* XRD setup limitations and bending of FTO coated glass at higher temperatures, accurate measurements could not be performed above 500 °C. It is clearly visible though that the last temperature regime does not stop suddenly at 500 °C, but continues at higher temperatures. Indeed, Gualtieri and Venturelli[58] evidenced by thermogravimetry that the weight loss due to water release continued up to 800 °C for the goethite–hematite phase transformation. By analogy and extrapolation, we conclude therefore that increasing the annealing temperature above 500 °C results in further transformation of the hematite phase by OH loss following the ordered aggregation mechanism.

Photoelectrochemical activity, photoanode efficiency

Using the protocol exhaustively detailed in the Methods section, the PEC activity of the hematite based photoanodes was fully characterized by determining the fast sweep photocurrent – $J_{ph}(V)$, fast sweep ON–OFF photocurrent – $J_{ph}^{ON-OFF}(V)$, stabilized photocurrent – J_{ph}^{stab}, quantum efficiency – IPCE(λ), photovoltage – V_{ph} and onset potential – V_{onset}.

Photocurrent and IPCE data are presented in Fig. 3 for all the samples. Pure hematite photoanodes are characterized using photocurrent values in the μA cm^{-2} range. Transients are more important for pure hematite samples annealed at 500 °C (S1) than at 600 °C (S2). From the IPCE curves (Fig. 3a and b) we extract higher efficiencies for sample S2. This is clearly related to lower transients in sample S2 (*i.e.* more important stabilized photocurrents) promoted by higher annealing temperature. Indeed, it is known that photocurrent can be enhanced by varying the air-annealing parameters like temperature, time and rate. Pyeon *et al.*[29] showed that the photocurrent of hematite photoanodes was improved by an oxygen plasma surface treatment followed by a short annealing. The same effect was reported by Hu *et al.*,[28] who interpreted this effect as arising from oxygen vacancy surface states at the as-grown hematite surface and, therefore, the existence of Fe^{2+} species at the photoanode surface. The density of the surface states was diminished after oxidizing the hematite films with oxygen plasma treatment. By analogy, this would suggest that in our case, when the air-annealing temperature is increased, the concentration of existing oxygen vacancies decreases and as a consequence the concentration of the associated reduced

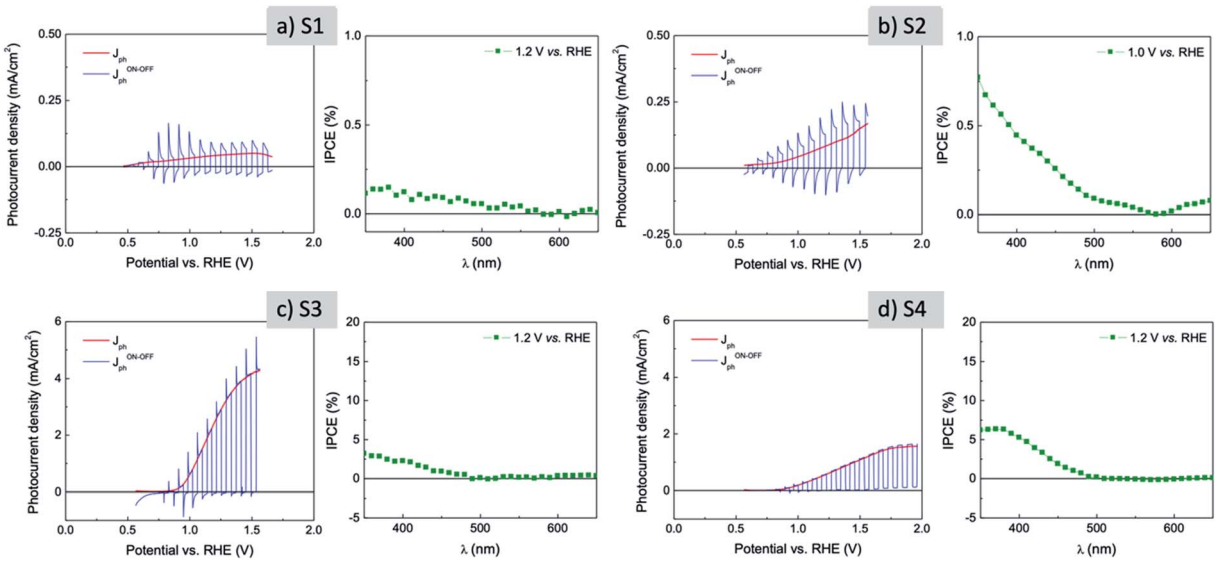

Fig. 3 Fast sweep photocurrent ($J_{ph}(V)$ red curves and J_{ph}^{ON-OFF} blue curves) and IPCE(λ) (green curve) obtained on S1 (a), S2 (b), S3 (c) and S4 (d) samples.

surface states (RSS) decreases, neutralized by oxygen from the air. Reduced Fe^{2+} species will be oxidized to Fe^{3+}, thus increasing the corresponding oxidized surface states (OSS). The OSS induce higher reactivity toward water oxidation than RSS,[28] with no transients on the $J_{ph}(V)$ curves and higher PEC efficiencies.

Fig. 3c–d show that Ti-substituted samples have higher photocurrents than pure hematite ones. Similar to pure hematite samples, Ti substituted samples annealed at 500 °C have important transients and, consequently, low IPCE values. Also, when the air-annealing temperature was increased from 500 °C to 600 °C, the transients disappear and the efficiencies increase. It appears that, like pure hematite, the oxygen vacancies on the surface are filled by oxygen upon air-annealing, thus preventing transient photocurrents.

Fig. 4 presents the fast-sweep $J_{ph}(V)$ and IPCE values obtained at 400 nm for all the samples. As mentioned before, we observe a converse behavior between the values of the photocurrent (hatched bars) and IPCE (full bars). Thus, sample S3 has the highest photocurrent while sample S4 has the highest IPCE. In $J(V)$ measurements the voltage is swept with a rate of 50 mV s^{-1}, faster than IPCE measurements where the current is stabilized for 200 s before the wavelength sweep starts. For this reason, IPCE provides a "time-stabilized" measurement of the photocurrent as a function of the wavelength. When transients are important, stabilized photocurrent values are lower (sometimes much lower) than the ones measured using a fast sweep $J_{ph}(V)$ measurement. Therefore, the photocurrent values are overestimated for the samples presenting high transients (S1 and S3), and reliable values are obtained only for the S2 and S4 samples. For all samples the transients observed for the sets annealed at 500 °C disappear for the 600 °C annealed counterparts, leading to higher IPCE values related to fewer oxygen vacancies and thus fewer RSS. Therefore, we conclude that the best photoanode is sample S4 since it has the highest IPCE value.

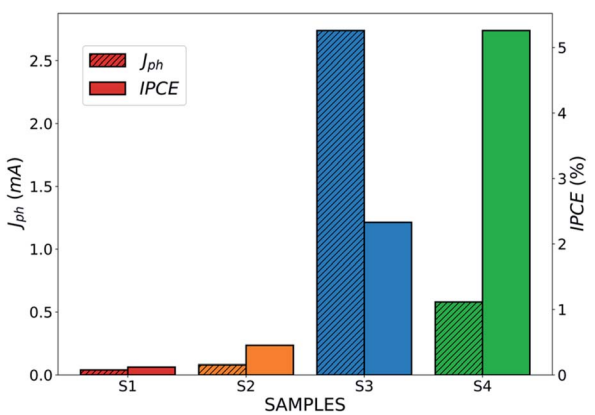

Fig. 4 Photocurrent (hatched bars) and IPCE (full bars) values recorded at 400 nm and 1.2 V for samples S1, S3, and S4 and 1.0 V for S2, respectively.

The onset potential, V_{onset}, *i.e.* the minimum potential at which photoelectrolysis occurs, and the photovoltage induced upon light absorption are two major parameters to take into account for the PEC activity. High photovoltages and low onset potentials positively favor the PEC activity. The onset potential can be extracted from the $J_{ph}(V)$ curve but, as mentioned by Iandolo *et al.*,[22] different methods may and should be used to determine its value more precisely. A first estimation of the onset potential for all the samples can be performed on the curves presented in Fig. 3. We observe that it is lower for pure hematite (~0.6 V *vs.* RHE) than for Ti-substituted samples (~0.8 V *vs.* RHE). However, for pure hematite the precision of this estimation is low because the photocurrent values are low. Therefore, a more precise value of the onset potential was determined by open-circuit potential experiments, as detailed in the Methods section. This approach allows us to measure

both photovoltages and onset potentials. The open-circuit voltages measured in the dark (V_{OFF}^{OC}) and under light (V_{ON}^{OC}) are represented by black and green bars, respectively, in Fig. SI-4† for the S1 and S4 samples. The precise value for the onset potential was 0.7 V *vs.* RHE for the pure hematite sample (S1) and 0.8 V *vs.* RHE for the Ti-substituted hematite sample (S4). We observe, like Niu *et al.*,[64] that Ti doping increases the onset potential, which is not favorable for a high PEC efficiency. In contrast, Miao *et al.*[24] found that for high Ti doping levels the onset potential decreases. They explained this result with the formation of a mixture of anatase and rutile TiO_2 on the surface of the films. In our case, we did not observe the formation of any TiO_2 in Ti-substituted hematite samples, as demonstrated later from the STXM measurements. Moreover, in the pure hematite sample (S1) we observed that the photovoltage is one order of magnitude higher (0.2 V for S1) than in the Ti-substituted sample (0.02 V for S4). However, despite favorable onset potential and photovoltage values for pure hematite samples, the experimental results show very clearly that the photocurrent and the efficiency are substantially improved in Ti-substituted samples. Thus, it appears that the effect of photovoltage and onset potential on the overall PEC activity in hematite-based photoanodes is not large. Indeed, it was shown that electrical conductivity is a key parameter for SWS efficiency. This is consistent with Ti-substituted samples having higher electrical conductivity than pure hematite[4] due to higher carrier concentration (n-type doping) and increased diffusion length.

Flat band estimations (EIS)

Nyquist plots obtained for a wide range of V_0 voltages for samples S1 and S4 are shown in Fig. SI-5 and SI-6.† First of all, we observe higher impedance values, in the kΩ range, for the pure hematite sample (S1) as compared to those for the Ti substituted one (S4), which are in the Ω range. This is undoubtedly related to the improved electrical conductivity upon Ti substitution of the hematite photoanodes. As detailed in the Methods section, the Nyquist plot slope gives a direct indication of the capacitive behavior at the interface with the electrolyte. Further discussion is supported by Fig. SI-5,† which presents a set of Nyquist plots at voltages ranging from 0.6 to 1.6 V recorded for the S1 sample. We distinguish four regions as a function of the applied voltage:

(i) $V_0 < 0.7$ V – typically, for low voltages below the flat band potential, the slope associated with the formation of the Helmholtz layer at the electrolyte interface is missing;

(ii) $0.7 < V_0 < 0.9$ V – the V_0 reaches the flat band value, V_{fb}, when no band-bending is expected inside the semiconducting photoanode and therefore there is no charge accumulation at the photoanode/electrolyte interface;

(iii) $V_{fb} < V_0 < 1.5$ V – this range can be assigned to the formation and evolution of the Helmholtz layer as the applied voltage increases. Charge accumulation is amplified at both sides of the interface, with holes inside the photoanode and negative charges in the electrolyte. During this regime, the slope associated with the Helmholtz layer is steep indicating a capacitive character, with no ion diffusion.[43]

(iv) $V_0 > 1.5$ V – further increasing the applied voltage results in a reduction of the slope value, related to the establishment of ion diffusion through the capacitive layer. Remarkably, this ion diffusion can be correlated to the slight decrease of the photocurrent within this applied voltage regime recorded for the S1 sample, as can be seen in Fig. 3a and SI-4.†

For the S4 sample the delimitation between the SC and Helmholtz contributions to the Nyquist plot is less obvious (see Fig. SI-6†) because Ti-substituted samples are characterized by lower impedances. Indeed, Ti substitution increases the electrical conductivity of the SC in contact with the electrolyte and thus, R_{SC} decreases (by a factor of 5 between S1 and S4), while the capacitance C_{SC} increases by a factor of 100, as deduced from Fig. 5. Nyquist plots for high and low impedances were modeled and the results are presented in Fig. SI-7.† Modeled Nyquist plots reproduce the experimental ones obtained for S1 and S4 samples very well. Similar to sample S1, we can identify the four different regions: (i) and (ii) for $V_0 < 0.3$–0.4 V; (iii) for $V_{fb} < V_0 < 1.0$ V and (iv) for $V_0 > 1.0$ V.

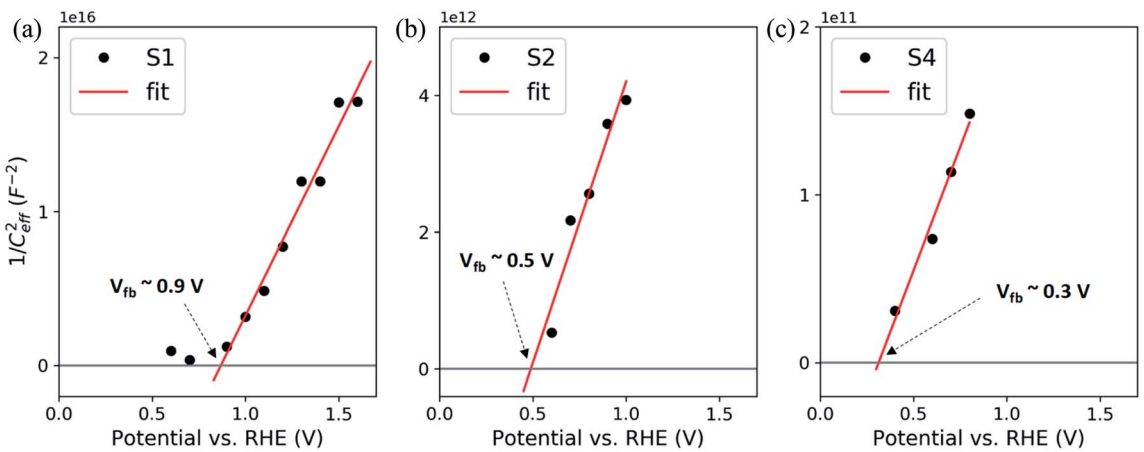

Fig. 5 Mott–Schottky plots for samples S1 (a), S2 (b) and S4 (c) representing $1/C_{eff}^2$ as a function of the applied voltage. The deduced flat band values for each sample are indicated.

EIS data were fitted using Python scripts to model the SC–electrolyte interface with the equivalent circuit presented in Fig. SI-3.† In general, different types of surface states related to structural defects may (co-)exist at the hematite/electrolyte interface. In our case, there are two types of surface states, RSS and OSS. RSS render the photoanode surface in contact with the electrolyte positively charged. By air-annealing, oxygen vacancies are filled with oxygen from the air. Therefore, the surface becomes less positively charged, even neutral. It was shown[49,50] that an S-shaped Mott–Schottky characteristic, $1/C_{\text{eff}}{}^2 = f(V)$, is expected in the presence of both positive and negative charged surfaces, a flat region appearing since surface states pin the Fermi level when the bias voltage varies. Positively or negatively charged surfaces will determine shifts to the right or to the left of the Mott–Schottky characteristic, resulting in higher or lower flat band values, respectively. Mott–Schottky plots obtained for samples S1, S2 and S4 are presented in Fig. 5. Linear fits of the experimental $1/C_{\text{eff}}{}^2$ data allow us to determine the flat band value (V_{fb}), which is indicated on each graph. We observe that V_{fb} is much higher for sample S1 (0.9 V) than for samples S2 (0.5 V) and S4 (0.3 V). This is due to a more positively charged S1 sample surface than for samples S2 and S4, undoubtedly related to the presence of RSS for sample S1 and OSS for S2 and S4 due to increased annealing temperatures.

Stoichiometry, chemical homogeneity, doping and electronic structure

Both surface (XPS) and bulk (STXM) approaches were employed to determine the chemical and electronic structures of the hematite photoanodes. Fig. SI-8† shows the Fe 2p (a) and Ti 2p (b) core level XPS spectra of the Ti-substituted hematite sample, S4. The characteristic Fe^{3+} shake-up satellite, visible at a 719 eV binding energy, confirms the formation of the α-Fe_2O_3 phase.[65] The Fe 2p and Ti 2p spectra are similar to those obtained by Zhao *et al.*[66] on 50 nm thick Ti:α-Fe_2O_3 films obtained by molecular beam epitaxy. The Ti 2p spectrum shows two narrow features located at 458.1 eV and 463.9 eV binding energies corresponding to Ti $2p_{3/2}$ and Ti $2p_{1/2}$ transitions, respectively. If the Ti $2p_{3/2}$ peak corresponding to Ti^{4+} in TiO_2 occurs at 458.8 eV,[67] the presence of Ti^{3+} should be represented by a peak at lower binding energy, 457.1 eV, inducing a wider Ti $2p_{3/2}$ peak. Like in ref. 66, this suggests that the valence of titanium in our samples is Ti^{4+}, and since the Ti 2p lines are narrow, we can conclude that there is no formation of Ti^{3+}. Interestingly, a rough estimate of the Ti content gives quite high values, at least higher than expected, of almost 32% in the hematite phase, compared to the 6% measured in the akaganeite phase. A segregation of Ti ions toward the surface of the nanorods could be at the origin of this significant difference.

XPS is a surface analysis technique, which only probes the outermost sample surface (<3 nm). Since our samples are thicker (hundreds of nanometers), there is no direct proof that the chemical composition and structure are homogeneous across and along the nanorods. We want to underline here that more and more studies exhibit XPS results as a confirmation of a certain expected electronic structure in very structured or thick samples. If the findings may be right over the entire depth of their samples, the reported XPS data cannot serve as a demonstration. To characterize the bulk stoichiometry, chemical homogeneity, substitution level and electronic structure of our samples, we employed STXM (X-ray absorption microscopy with a ~60 nm spatial resolution).

Since STXM relies on the XAS sensitivity measured in transmission geometry, the extent of Ti substitution can be estimated by reproducing the optical density of the elemental components in the range from 450 eV to 850 eV through the linear absorption energy dependent coefficient, μ, as:

$$\mu = 2\lambda \times r_0 \times \sum(n_{\text{at}} \times f_{2_{\text{at}}}) \quad (9)$$

where λ is the X-ray wavelength, r_0 is the classical electron radius, n_{at} is the atomic number density and $f_{2_{\text{at}}}$ is the imaginary part of the atomic scattering factor.[68] To obtain the energy dependence of μ we recorded energy stacks (3D datasets) tuning the X-ray energy from 450 eV to 850 eV covering all edges of interest: Ti $L_{2,3}$, O K and Fe $L_{2,3}$, as presented in Fig. 6. It is important to mention that for this part we performed measurements on sample chunks on TEM grids, prepared as described in the Experimental section. The results can be compared to spatially averaged XAS measurements reported in the literature on similar samples.[33] The XAS spectrum of sample S4 plotted in Fig. 6b was obtained as follows: first, the 3D dataset was aligned (to account for sample drift during data collection) and transformed into optical density (OD) using aXis2000 software. Second, the drift-corrected energy stack was processed using PCA (Principal Component Analysis) and CA (Cluster Analysis) implemented in MANTIS software in order to identify spatial regions with spectral similarities. The result of the PCA–CA analysis is shown in Fig. 6a along with the corresponding SEM and STXM images. Third, the choice of the cluster to be used for elemental analysis was made such as to avoid both absorption saturation and border regions, where the spectra are affected by strong thickness effects. In this manner, the "red" cluster for the S4 sample, which has the "red" data spectrum in Fig. 6b, was chosen. The black curve is the fitted atomic continuum signal, following the formula (eqn (7)). The variable parameter in the fit was the atomic number density, n_{at}, through the chemical formulation expressed as a variable function of the Ti content, x, like Fe_xTi_{1-x}, assuming substitutional doping for the Ti. In addition to the doped hematite ($Fe_{2x}Ti_{2-2x}O_3$), we introduced the stoichiometric iron chloride hexahydrate phase ($Fe_xTi_{1-x}O_6H_{12}Cl_3$) which is present as a precursor in the aqueous solution, and we assumed the same Ti substitution in both iron-oxide phases. The necessity of using both iron-oxide phases arises from uncertainties of the scattering factors, in particular at the L edges. Indeed, Le Guillou *et al.*[69] demonstrated that even in the case of K edges (there the C, N, and O), where the tabulated scattering factors are more accurate, direct quantification is difficult. They proposed a methodology based on spectral deconvolution and normalization with respect to C/N atom ratios determined from reference samples. Such a methodology is well beyond the scope of this study and here we simply used the iron chloride

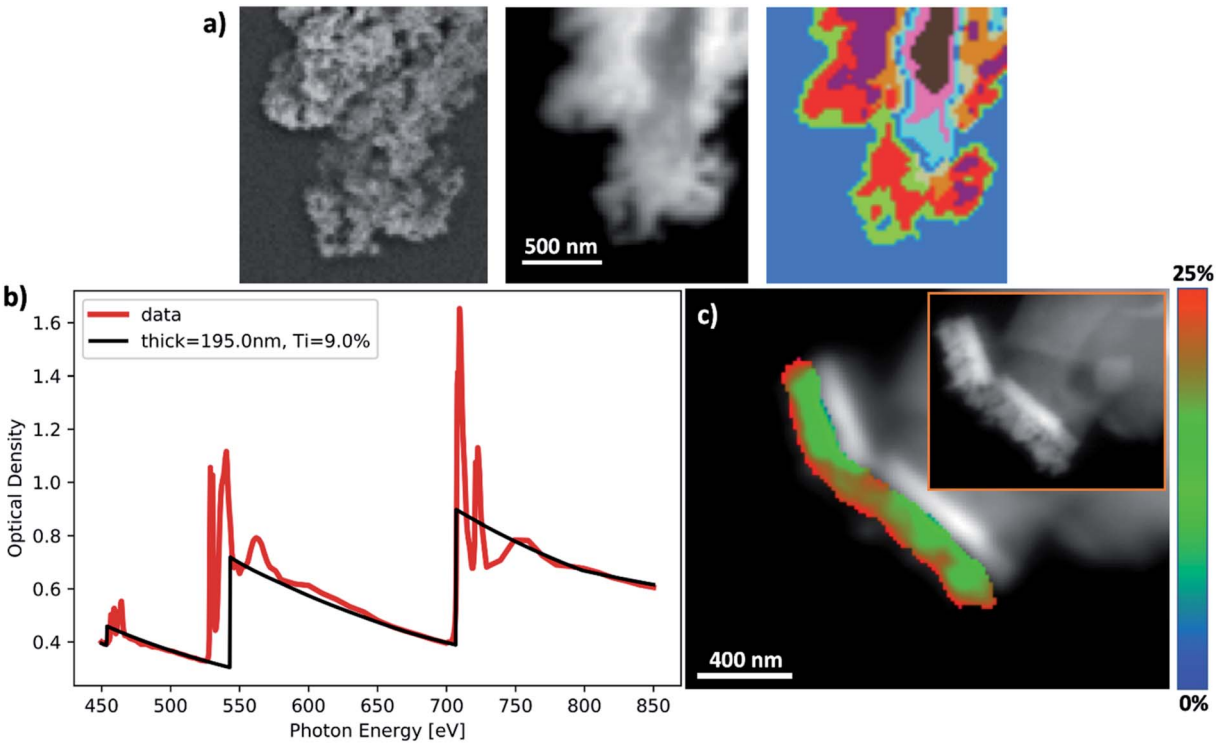

Fig. 6 (a) From left to the right: SEM, STXM (at 709.6 eV) and cluster analysis images of the same sample region. (b) Determination of the Ti content from the STXM data for the S4 sample. The experimental spectrum (data) is from the red region indicated in the associated cluster analysis results shown in (a). The black curve represents the fitted elemental signal used to derive the composition (9 at% TiO_2 in Fe_2O_3), as detailed in the text. (c) STXM map of the Ti substitution for the S4 sample. For clarity the color-coded map was obtained with a mask defined around the hematite layer and then superposed on the STXM OD image at 529.9 eV, shown in the inset of (c). The rainbow colored scale indicates the Ti at% composition in the nanorods.

hexahydrate contribution to reproduce a pure hematite commercial reference. As shown in Fig. 6b, this approach allows us to perfectly reproduce the XAS background. In addition, using the same Ti content in both phases provides a good estimation of the overall substitution level. We obtain ~9% Ti substitution for sample S4. At this point it is difficult to conclude anything about the spatial homogeneity of the Ti substitution in the hematite nanorods, as the used samples do not allow disentangling unambiguously different spatial regions, *i.e.* the interface or surface of the nanorods. Even when the same methodology is used to analyze other clusters after PCA–CA, we cannot exclude variations of the deduced Ti substitution level inside the hematite nanorods.

To obtain information about possible variations of the Ti content along the hematite nanorods we analyzed equivalent samples prepared by UMT, as shown in Fig. 6c. To produce the color-coded maps, we used a different approach than the one presented above, namely the stack fit (SF) procedure. Implemented in aXis2000 software, the SF procedure uses singular value decomposition (SVD),[70] a matrix method equivalent to a linear least squares fit, to fit the OD at each pixel to a linear combination of reference spectra and an additional constant contribution. Quantifying each individual component in the resulting chemical speciation map is possible using reference spectra which have been placed on an OD1 intensity scale, *i.e.* the optical density expressed for 1 nm thickness and bulk density. To apply the SF procedure, we measured two external references: a pure commercial hematite nano-powder (reference 544884 from SigmaAldrich) and a sample prepared from the $TiCl_3$-based precursor used during the ACG growth. In the first case, the hematite powder was dispersed in the dried state on a SiN membrane. In the second case, 3 μL of the $TiCl_3$-based precursor solution was drop cast directly on a SiN membrane and air-dried prior to transfer into the STXM microscope vacuum. Both reference spectra were reduced to OD1 units by fitting the thickness from the Beer–Lambert law (eqn (7)) and considering the bulk densities for hematite (5.3 g cm^{-3}) and $TiCl_3$ (2.64 g cm^{-3}). Applying SF analysis, we generated component maps in nm units for both hematite ($img_{Fe_2O_3}$) and Ti (img_{Ti}) components. The color-coded map presented in Fig. 6c, as % of Ti substitution, was obtained using:

$$img_{\%} = img_{Ti}/(img_{Ti} + img_{Fe_2O_3}) \quad (10)$$

The result of this analysis is consistent with the one using eqn (7) and applied to the equivalent samples showing a mean value of 9 at% Ti in S4. It is important to emphasize the presence of a Ti substitution gradient which is clearly highlighted in the color-coded images in Fig. 6c. The sample is characterized by lower Ti content toward the interface with the FTO substrate, suggesting surface segregation of Ti. This finding is consistent with our XPS results which give higher Ti/Fe ratios (32 at%) than

the ones determined from XAS. Nevertheless, no signs of metallic Ti or Ti oxide could be detected in the STXM measurements within the spatial resolution limit of ~60 nm.

Fig. 7, top panel, exhibits the normalized (at zero value for the pre-edge and 1 after the edge jump) Ti spectra recorded over the $L_{2,3}$ edges corresponding to 2p–3d electronic transitions for the S3 and S4 samples. We observe the expected alternating t_{2g} and e_g symmetries, split into two sets, the low energy (455–460 eV) L_3 and the high energy (460–465 eV) L_2, by the spin–orbit interaction of the Ti 2p core hole. The single narrow peak (marked with a red arrow) at ~459 eV is characteristic of Ti^{4+} ions in a perfect octahedral environment, as found in $FeTiO_3$ (ilmenite)[71] or $SrTiO_3$.[71–73] This suggests that the Ti^{4+} ions replace Fe^{3+} ones in the Fe–O_6 octahedron maintaining an octahedral coordination, with no clustering of rutile or anatase TiO_2. Therefore, the simple substitution method followed here gives similar results to the other reported Ti substitution methods.[33]

Interestingly, the S4 sample shows lower Ti content compared with S3, for which we determined ~12 at% Ti. As suggested by the XRD measurements which monitor the phase transformation from akaganeite to hematite, some of the Ti could be bonded directly with Cl in the Ti substituted akaganeite structure and thus subjected to removal by increasing the annealing temperature. The Fe $L_{2,3}$ absorption edges, shown in the ESI (Fig. SI-9),† are typical for hematite with Fe^{3+} ions in perfect octahedral coordination. We note that the transmission experiment at the Fe L-edge on our samples is very difficult due to the small attenuation length which is about 120 nm at the Fe L_3 peak (710 eV). In addition, Fe exhibits very strong resonances and considering the thicknesses of the STXM prepared samples, both directly by wiping or by UMT, it was very difficult to obtain spectra exempt from saturation effects.

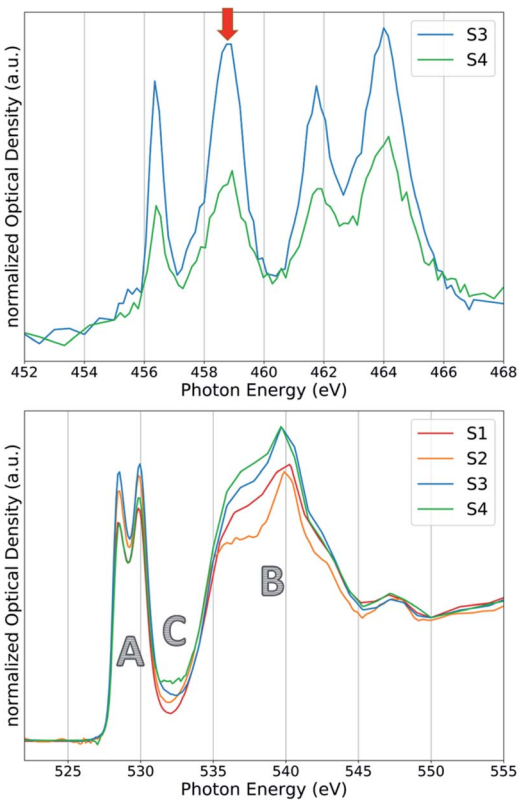

Fig. 7 Ti $L_{2,3}$ (top) and O K (bottom) spectra recorded by STXM. Curve colors, which indicate the sample, are the same in both graphs. The Ti L_{23} spectrum exhibits a $SrTiO_3$ like spectral shape, with a narrow, single (L_3, e_g) peak at 459 eV, for all the samples measured here. The O K spectrum presents very rich spectral features following the A, B and C notations, which are discussed in the text.

The oxygen K edge XAS spectral region carries rich information about the electronic conduction properties of oxide materials, due to the delocalized character of the O 2p orbitals extending over several atomic sites.[74] Strong O 2p–TM (transition metal) 3d orbital hybridization appears in this spectral region.

We distinguish three spectral regions, A, B and C, as indicated in Fig. 7, bottom panel. Region A–C contains overlapping O 1s → hybridized O 2p–TM 3d transitions, showing the t_{2g} and e_g symmetries. Region B corresponds to overlapping O 1s → O 2p and O 1s → hybridized O 2p–TM 4s4p transitions. Peak integrals, I, are proportional to the density of the unoccupied states and to the hybridization strengths, which are related to the degree of interaction between O 2p and TM 3d or TM 4s4p orbitals.[75] In the absence of any p–d hybridization, I_A should be zero because the dipole selection rule does not allow any s → d transition. Therefore, the ratio I_A/I_B is a direct indication of the hybridization strength in this system. The $I_{t_{2g}}/I_{eg}$ ratio is related to the crystal structure and should depend in the first approximation on the number of unoccupied d-orbitals. Generally, for an octahedral symmetry of oxygen ligands, this ratio is 3/2. For hematite, this ratio is lower than 1 due to a diminished hybridization as shown by de Groot et al.[76] The crystal field splitting, calculated using $\Delta_0 = E_{e_g} - E_{t_{2g}}$ is 1.4 eV, is in agreement with the expected value for hematite.[76] The dispersion of the TM 3d band, reflected by the full width at half maximum (FWHM) of peak A, is constant for all the samples considering the Lorentzian broadening due to the core-hole lifetime being ~0.2 eV.[74] The energy of peak B (the relevant parameter is the relative position of peak B with respect to t_{2g}: $\Delta E_B = E_B - E_{t_{2g}}$) is related to the effective interaction between O 2p and TM sp states. The covalent character of the oxide (the contribution of covalent bonding to the hybridization strength) is defined by the ratio I_A/I_B. Upon Ti substitution and similarly to the different Ti doping or substitution methods collected in the review published by Kronawitter *et al.*,[33] we distinguish an evolution of the O K-edge absorption spectra (Fig. 8) related to the formation of new O 2p hybridized states by mixing new Ti s and d states in the hematite conduction band.

To go further, quantitative analysis was performed by deconvoluting the O K-edge spectra[77] considering the electronic transitions described above. In this regard, we used an arctangent background and a series of pseudo-Voigt peaks centered on the experimental spectral features. The position of the arctangent step background was set to 534 eV, as in other similar reports.[78–80] During the fitting adjustments all Lorentzian fractions converged to very small values, the Gaussian part being largely dominant, supporting the choice of pure Gaussian line-shapes as often

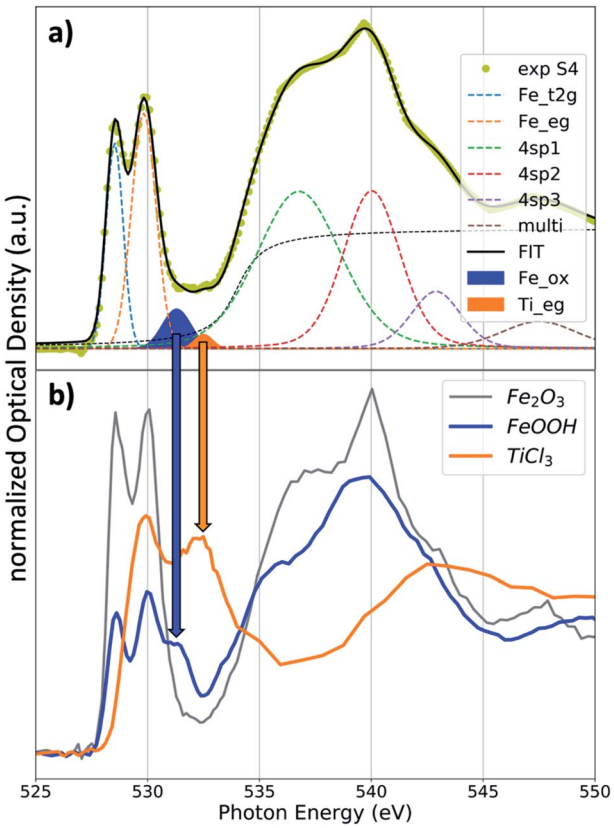

Fig. 8 (a) Peak fitting analysis of the O K-edge spectrum of Ti substituted hematite (S4). Arctangent background and fitted peaks are indicated. (b) Reference O K-edge spectra of akaganeite, pure hematite and $TiCl_3$. Blue and orange arrows indicate the peak positions corresponding to akaganeite and the respective Ti e_g transitions.

made in other reports.[80,81] Fig. 8a, top panel, presents the fit for sample S4 (all fits are reported in Fig. SI-10†) as a typical example of the deconvolution. For direct comparison, Fig. 8b, lower panel, plots a reference akaganeite O K spectrum obtained from a sample before the annealing process and the oxidized $TiCl_3$ reference as they present particular spectral features as further described below. We used several distinct spectral contributions as follows. In region A–C we identified four peaks at 528.5 eV (Fe t_{2g}), 529.9 eV (Fe e_g and Ti t_{2g}), 531.35 eV (blue peak) and 532.65 eV (Ti e_g, orange peak). The third (blue) peak, that we named Fe-ox, corresponds to the energy position in the akaganeite phase as indicated in Fig. 8 by the blue arrow. Its energy is shifted by +1.45 eV with respect to the Fe e_g from hematite, in agreement with several studies on goethite.[81,82] This corresponds to electronic transitions from the O 1s of hydroxide to hybridized Fe 3d bands. A peak corresponding to the hybridized Sn 5s–O 2p arising from the FTO substrate is expected at around 532.5 eV as shown by Kronawitter *et al.*[83] and by our XAS measurements obtained on a bare FTO substrate (Fig. SI-11†). Nevertheless, this peak was not observed on pure hematite samples (S1 and S2), and its presence is uncertain for Ti-substituted samples (S3 and S4), since its spectral position coincides with the Ti e_g peak (orange arrows on Fig. 8). We assign it therefore strictly to the Ti e_g contribution. In region B, four additional peaks were used to account for the contributions of the 4sp band below 545 eV (ref. 76) and multiple scattering resonant features of the O^{2-} ions, above 545 eV.[81]

Fig. 9 depicts the results of the deconvolution of the O K-edge spectra of all 4 samples. First, we discuss the evolution of the Fe-ox peak (full bars in Fig. 9). As argued above, this spectral position could be related to the electronic transition from the hydroxide O 1s to hybridized Fe 3d level. However, its intensity increases with the temperature from the S1 to S2 and S3 to S4 samples which rules out the hypothesized origin, since higher annealing temperatures decrease the oxyhydroxide content as shown by the XRD results. Therefore, we suggest that part of its spectral weight arises from a higher oxidized Fe state appearing at higher energies with respect to the Fe e_g. Furthermore, we believe that this peak could be a signature of the presence of empty oxidized surface states (OSS), though not as oxidized as those reported by Bora *et al.*[78] arising from the hematite photoanode electrochemical oxidation in KOH and at an applied potential of 600 mV. These authors focus their discussion on the new obvious peak at 532.7 eV, considering the peak at 531.7 eV, similar to our OSS, simply as an additional unassigned fit component. Interestingly, this peak is reported in the O K-edge spectrum of a nano-powder Fe_2O_3 sample. Hence, it appears to be a feature related to the nanostructured nature of the sample. Indeed, the same feature was clearly identified by Ye *et al.* Fe_2O_3 (ref. 80) in their hematite samples obtained by atomic layer deposition and solution-based regrowth methods. In addition, an evolution of the weighted spectral intensity of the C region in the O K-edge spectra was reported in a size-dependent study of hematite nanoparticles.[84] In that report there is a significant increase of the peak intensity with decreasing particle size. Therefore, this supports our interpretation of the additional Fe-ox spectral contribution as an oxidized surface state contribution, OSS, related to the nanostructured carpet-like morphology and even more to the aggregated crystalline structure as identified by XRD. So, the increase of the OSS from S1 to S2 and S3 to S4 is explained by

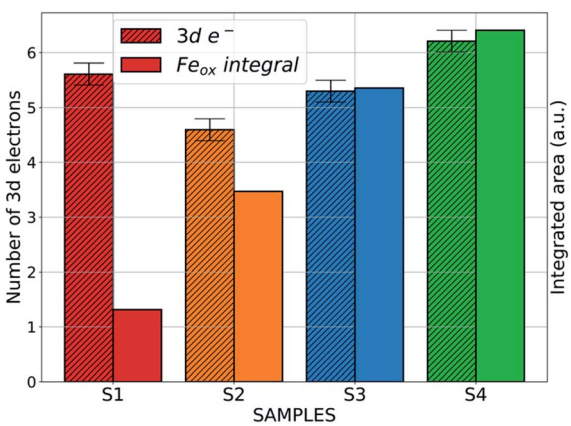

Fig. 9 Number of 3d electrons (hatched bars) and integrated Fe-ox area (full bars) for the four samples, from S1 to S4. Details about the estimation of the number of 3d electrons are given in the text. The same colour coding as in Fig. 4 and 7 is used.

stronger oxidation at 600 °C than at 500 °C. The strong increase upon Ti incorporation deserves further discussion. In their pioneering work using soft X-ray XAS and ultrafast transient absorption spectroscopy, Kronawitter *et al.*[85] observed a peculiar electronic structure at the hematite/titanium oxide interface characterized by a different d–p orbital hybridization compared to both hematite and Ti oxide reference single crystals. They assigned this unusual electronic structural feature to the occurrence of an interfacial electron enrichment, *i.e.* increase of the 3d electron number at the junction between the two nano-heterostructures. For this purpose, they measured several reference single crystals and made a linear fit to the ratio of the 3d and 4sp bands as a function of the 3d electron number. In more recent work,[86] Ye *et al.* proposed a similar dependence measuring different TM oxides. To estimate the number of 3d electrons, we first sum the fitted Fe t_{2g}, Fe e_g and Ti e_g contributions from the A–C spectral regions and the three 4sp contributions from the B region, excluding the last one at 547 eV which corresponds to a multiple scattering contribution. The results in Fig. 9 (hatched bars) are obtained applying the above-mentioned linear dependence to this ratio. We report here the median value from the two references and consider their discrepancy relative to the measured 3d–4sp ratio in setting the error bar. While the estimated number of 3d electrons is very close to the expected 5 electrons for Fe^{3+} for the S1–S3 samples, this analysis for the S4 sample suggests that it has more than 6 electrons in the 3d band, reaching the same value as that reported for Ti_xO_y–Fe_2O_3 heterostructures.[85]

Fig. 9 shows that upon Ti substitution, two concomitant phenomena act together to benefit the PEC activity. First, the 3d bands exhibit an increased number of charges participating in the electric conduction. Second, the highly oxidized character of the OSS will promote charge transfer from the electrolyte. Comparing the Fe-ox integrals from Fig. 9 and the IPCE values from Fig. 4 it appears that the efficiency of the PEC activity scales directly with the hole occupancy in the OSS. It was shown[33] that the effect of Ti incorporation into the conduction band of hematite is more pronounced toward the surface region irrespective of the synthesis technique. This is particularly true in our study where the OSS are strongly promoted by the Ti substitution. Moreover, as shown in Fig. 6, there is a visible Ti gradient toward the surface of the film, suggesting an increased Ti-driven conduction band modification at the surface.

From the information gained we can propose the mechanism behind the OSS driven PEC enhancement. As XAS directly probes the density of states (DOS) of the SC unoccupied levels, *i.e.* the conduction band (CB), it is more convenient to represent the energy diagram at the SC/electrolyte interface, Fig. 10, following the Gerischer model.[87,88] In this case, the redox couple of the electrolyte is expressed as a reduced/oxidized distribution of states (in terms of density of states) equally separated at a value given by the activation energy (not shown here) around the redox potential, E_{redox}. At equilibrium, the E_F of the SC is aligned with the E_{redox} of the NaOH electrolyte. Following the Gerischer model, in the case of an n-type SC in contact with the electrolyte, equilibrium is reached by electron transfer from the electrolyte into the SC conduction band. The rate constant for

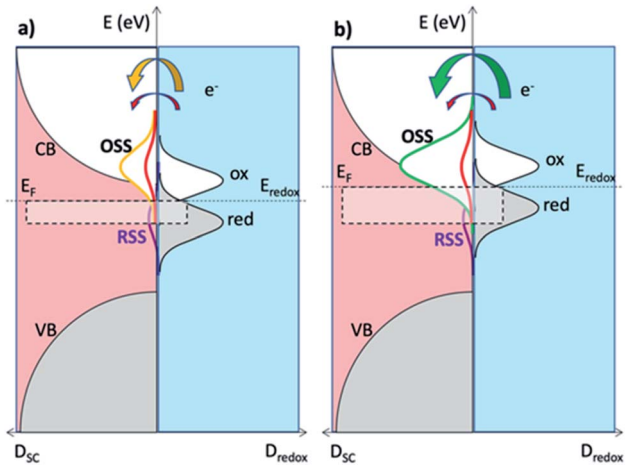

Fig. 10 Energy diagram at equilibrium of the SC/electrolyte interface following the Gerischer model expressing the electrolyte redox couple in terms of the reduced/oxidized DOS couple. The effect on the OSS DOS and resulting enhanced photocurrent upon increasing the annealing temperature (a) and Ti substitution (b) are shown. For the sake of clarity the OSS associated DOS is exaggerated compared to the CB. In addition, the color coding is the same as for the other figures: red – sample S1, orange – sample S2 and green – sample S4.

the electron transfer (and thus the photocurrent) is proportional to the overlapping of the filled states from the SC with the ones in the electrolyte. In other words, increased DOS of the available filled surface states will lead to increased photocurrent under PEC conditions. It is important to mark the clear distinction between the OSS and RSS in this diagram. With the XAS results only, we cannot precisely locate the RSS when they are lying below E_F, (since filled states are "invisible" to the XAS measurements). Nevertheless, the PEC results clearly evidenced their presence for the S1 sample through the very important measured transient photocurrents, as shown. In order to produce a net stabilized photocurrent, the electrons from the RSS should reach the CB, provided that RSS overlap with the CB. Otherwise, RSS will act as trapping centers promoting charge recombination and low stabilized photocurrents. Our results for sample S1 show clearly that RSS act mainly as trapping centers during the photoelectrolysis suggesting thus that they are lying bellow the CB minimum, and the overlapping between the RSS and the CB is low. In Fig. 10a we show the increase of the OSS DOS from S1 (red) to S2 (orange) as determined from the STXM (XAS) measurements (see Fig. 9). The region overlapping with the electrolyte redox levels is indicated by the gray rectangle just below the EF. The same mechanism is indicated in Fig. 10b, where the effect upon Ti substitution is even more visible, with a larger increase of the corresponding OSS DOS, as given by the results shown in Fig. 9. In this case the effect is amplified by the shift of the E_F level toward the CB, due to the Ti substitution which results in a stronger n-type character of the hematite.

Conclusions

Hematite (including Ti substituted hematite) photoanodes shaped like carpet-like films of ordered nanorods were

successfully produced using aqueous chemical growth from chloride precursors. The photoelectrochemical (PEC) efficiency increases with the Ti substitution and the annealing temperature. Strong transient photocurrents and reduced incident photon-to-current efficiency were found to originate from oxygen vacancies present when annealing at lower temperatures. The PEC activity is improved by increasing the annealing temperature, due to the occurrence of oxidized surface states as revealed by X-ray absorption spectroscopy. Oxygen vacancies and associated reduced surface states (RSS) induce higher flat-band values than oxidized surface states (OSS). The experimental methodology needed for measuring meaningful photocurrent values was identified. *In situ* X-ray diffraction (XRD) revealed the crystallization mechanism and an intimate relationship between annealing temperature and the resulting micro-structure and morphology. In particular, XRD confirmed that Ti inhibited nanorod growth in Ti substituted hematite photoanodes and suggested the existence of two kinds of Ti in the structure: some in substitution of Fe inside $Fe–O_6$ octahedra, and some bonded with Cl from the "tunnel" akaganeite structure. Electrochemical impedance spectroscopy was used to measure flat band potentials and to determine ion diffusion in the Helmholtz layer for voltages higher than 1.5 V, in agreement with the photocurrent decrease.

Our study highlights three major facts. First, we provided evidence that surface states affect PEC efficiency. In particular there are RSS, originating from oxygen vacancies, which are counterbalanced by OSS, originating from enhanced hematite oxidation. The extent of each type of surface state varies as a function of the annealing temperature applied during the akaganeite to hematite phase transformation. Indeed, during the phase transformation, the ordered aggregation crystallization mechanism leads to a peculiar microstructure inside the hematite nanorods, offering conditions for promoting either reduced or oxidized surface states as a function of the temperature. Moreover, we demonstrated that surface states affect other parameters like the photovoltage and the onset potential for enhanced PEC performance. Second, we successfully disentangled the effects of electronic conduction enhancement from surface state effects upon Ti substitution. We demonstrated that these are concomitant and not exclusive effects, as largely suggested until now. Third, we used synchrotron X-ray spectromicroscopy to corroborate our findings. In particular we observe a Ti substitutional gradient explaining the surface enhanced conduction band modification. Finally, we demonstrated that the best performing hematite-based photoanodes rely on both composition (Ti substitution) and surface state engineering.

Further development of our study should be conducted on highly optimized hematite-based photoanodes, in particular those using efficient oxygen evolution catalysts (for instance in ref. 89 and 90). In this case the strongly modified surface states can highlight valuable additional paths with respect to the present study offering further improvement of the PEC activity.

Author contribution

D. Stanescu and S. Stanescu conceived the study, conducted the SEM, PEC and STXM measurements and analyzed the data. V. Villard and M. Piriyev prepared the samples and performed the PEC and synchrotron STXM measurements as part of their master's thesis work. C. Mocuta carried out the synchrotron *in situ* XRD measurements and analyzed the associated data. J. Leroy performed the XPS measurements. D. Ihiawakrim and O. Ersen developed the UMT protocol and performed the preliminary TEM characterization of related samples. A. Besson initiated the SEM measurements. S. G. Chiuzbaian and A. Hitchcock participated as experts in the STXM (XAS) analysis and in the master's students' training. D. Stanescu and S. Stanescu wrote the paper. All authors participated in the reading of the paper and its improvement.

Conflicts of interest

There are no conflicts to declare.

Acknowledgements

We acknowledge Anne Forget from the SPEC and Karine Chaouchi and Stephanie Blanchandin from the SOLEIL synchrotron for technical support in the respective chemistry laboratories. We thank the Synchrotron Soleil for providing beam time for this study, both at the DiffAbs (XRD) and the HERMES (STXM) beamlines, and the HERMES staff for expert support with the STXM instrument. Adam Hitchcock thanks the SOLEIL synchrotron staff for providing support during several visits. Maëva L'Heronde from the IPANEMA laboratory is acknowledged for her assistance during the SEM measurements.

References

1 A. Fujishima and K. Honda, *Nature*, 1972, **238**, 37–38.
2 Z. Li, W. Luo, M. Zhang, J. Feng and Z. Zou, *Energy Environ. Sci.*, 2013, **6**, 347–370.
3 K. Sivula, F. Le Formal and M. Grätzel, *ChemSusChem*, 2011, **4**, 432–449.
4 M. Rioult, H. Magnan, D. Stanescu and A. Barbier, *J. Phys. Chem. C*, 2014, **118**, 3007–3014.
5 C. A. Bignozzi, S. Caramori, V. Cristino, R. Argazzi, L. Meda and A. Tacca, *Chem. Soc. Rev.*, 2013, **42**, 2228.
6 B. S. Kalanoor, H. Seo and S. S. Kalanur, *Mater. Sci. Energy Technol.*, 2018, **1**, 49–62.
7 A. Chemseddine, K. Ullrich, T. Mete, F. F. Abdi and R. Van De Krol, *J. Mater. Chem. A*, 2016, **4**, 1723.
8 M. Rioult, S. Datta, D. Stanescu, S. Stanescu, R. Belkhou, F. Maccherozzi, H. Magnan and A. Barbier, *Appl. Phys. Lett.*, 2015, **107**, 103901.
9 Z. Chen, T. F. Jaramillo, T. G. Deutsch, A. Kleiman-Shwarsctein, A. J. Forman, N. Gaillard, R. Garland, K. Takanabe, C. Heske, M. Sunkara, E. W. McFarland,

K. Domen, E. L. Miller, J. A. Turner and H. N. Dinh, *J. Mater. Res.*, 2010, **25**, 3–16.
10 R. Van De Krol and M. Gratzel, *Photoelectrochemical hydrogen production using visible light*, Springer, 2012, vol. 2.
11 R. Van De Krol, Y. Liang and J. Schoonman, *J. Mater. Chem.*, 2008, **18**, 2311–2320.
12 A. G. Tamirat, J. Rick, A. A. Dubale, W. N. Su and B. J. Hwang, *Nanoscale Horiz.*, 2016, **1**, 243–267.
13 J. A. Glasscock, P. R. F. Barnes, I. C. Plumb and N. Savvides, *J. Phys. Chem. C*, 2007, **111**, 16477–16488.
14 M. Rioult, R. Belkhou, H. Magnan, D. Stanescu, S. Stanescu, F. Maccherozzi, C. Rountree and A. Barbier, *Surf. Sci.*, 2015, **641**, 310.
15 C. X. Kronawitter, S. S. Mao and B. R. Antoun, *Appl. Phys. Lett.*, 2011, **98**, 092108.
16 S. C. Riha, B. M. Klahr, E. C. Tyo, S. Seifert, S. Vajda, M. J. Pellin, T. W. Hamann and A. B. F. Martinson, *ACS Nano*, 2013, **7**, 2396–2405.
17 L. Vayssieres, *Int. J. Nanotechnol.*, 2004, **1**, 1–41.
18 J. Y. Kim, G. Magesh, D. H. Youn, J. W. Jang, J. Kubota, K. Domen and J. S. Lee, *Sci. Rep.*, 2013, **3**, 2681.
19 K. Tolod, S. Hernández and N. Russo, *Catalysts*, 2017, **7**, 13.
20 C. Yilmaz and U. Unal, *RSC Adv.*, 2015, **5**, 16082–16088.
21 X. Lian, X. Yang, S. Liu, Y. Xu, C. Jiang, J. Chen and R. Wang, *Appl. Surf. Sci.*, 2012, **258**, 2307–2311.
22 B. Iandolo, B. Wickman, I. Zorić and A. Hellman, *J. Mater. Chem. A*, 2015, **3**, 16896–16912.
23 J. Zhang and S. Eslava, *Sustainable Energy Fuels*, 2019, **3**, 1351–1364.
24 C. Miao, T. Shi, G. Xu, S. Ji and C. Ye, *ACS Appl. Mater. Interfaces*, 2013, **5**, 1310–1316.
25 F. Le Formal, K. Sivula and M. Grätzel, *J. Phys. Chem. C*, 2012, **116**, 26707–26720.
26 X. Shi, K. Zhang and J. H. Park, *Int. J. Hydrogen Energy*, 2013, **38**, 12725–12732.
27 F. Le Formal, N. Tétreault, M. Cornuz, T. Moehl, M. Grätzel and K. Sivula, *Chem. Sci.*, 2011, **2**, 737–743.
28 Y. Hu, F. Boudoire, I. Hermann-Geppert, P. Bogdanoff, G. Tsekouras, B. S. Mun, G. Fortunato, M. Graetzel and A. Braun, *J. Phys. Chem. C*, 2016, **120**, 3250–3258.
29 M. Pyeon, T. P. Ruoko, J. Leduc, Y. Gönüllü, M. Deo, N. V. Tkachenko and S. Mathur, *J. Mater. Res.*, 2018, **33**, 455–466.
30 C. Du, X. Yang, M. T. Mayer, H. Hoyt, J. Xie, G. McMahon, G. Bischoping and D. Wang, *Angew. Chem., Int. Ed.*, 2013, **52**, 12692–12695.
31 P. Sharma, J. W. Jang and J. S. Lee, *ChemCatChem*, 2019, **11**, 157–179.
32 S. Shen, C. X. Kronawitter, D. A. Wheeler, P. Guo, S. A. Lindley, J. Jiang, J. Z. Zhang, L. Guo and S. S. Mao, *J. Mater. Chem. A*, 2013, **1**, 14498–14506.
33 C. X. Kronawitter, I. Zegkinoglou, S. H. Shen, P. Liao, I. S. Cho, O. Zandi, Y. S. Liu, K. Lashgari, G. Westin, J. H. Guo, F. J. Himpsel, E. A. Carter, X. L. Zheng, T. W. Hamann, B. E. Koel, S. S. Mao and L. Vayssieres, *Energy Environ. Sci.*, 2014, **7**, 3100–3121.
34 X. Liu, F. Wang and Q. Wang, *Phys. Chem. Chem. Phys.*, 2012, **14**, 7894–7911.
35 S. Basolo, J. F. Bérar, N. Boudet, P. Breugnon, B. Caillot, J. C. Clemens, P. Delpierre, B. Dinkespiler, I. Koudobine, C. Meessen, M. Menouni, C. Mouget, P. Pangaud, R. Potheau and E. Vigeolas, *IEEE Trans. Nucl. Sci.*, 2005, **52**, 1994–1998.
36 P. Pangaud, S. Basolo, N. Boudet, J. F. Berar, B. Chantepie, J. C. Clemens, P. Delpierre, B. Dinkespiler, K. Medjoubi, S. Hustache, M. Menouni and C. Morel, *Nucl. Instrum. Methods Phys. Res., Sect. A*, 2008, **591**, 159–162.
37 K. Medjoubi, T. Bucaille, S. Hustache, J. F. Bérar, N. Boudet, J. C. Clemens, P. Delpierre and B. Dinkespiler, *J. Synchrotron Radiat.*, 2010, **17**, 486–495.
38 C. Le Bourlot, P. Landois, S. Djaziri, P. O. Renault, E. Le Bourhis, P. Goudeau, M. Pinault, M. Mayne-Lhermite, B. Bacroix, D. Faurie, O. Castelnau, P. Launois and S. Rouzire, *J. Appl. Crystallogr.*, 2012, **45**, 38–47.
39 C. Mocuta, M. I. Richard, J. Fouet, S. Stanescu, A. Barbier, C. Guichet, O. Thomas, S. Hustache, A. V. Zozulya and D. Thiaudière, *J. Appl. Crystallogr.*, 2013, **46**, 1842–1853.
40 J. L. Hudson and T. T. Tsotsis, *Chem. Eng. Sci.*, 1994, **49**, 1493–1572.
41 X. S. Zhou, B. W. Mao, C. Amatore, R. G. Compton, J. L. Marignier, M. Mostafavi, J. F. Nierengarten and E. Maisonhaute, *Chem. Commun.*, 2016, **52**, 251–263.
42 L. M. Peter, K. G. U. Wijayantha and A. A. Tahir, *Faraday Discuss.*, 2012, **155**, 309–322.
43 B. A. Mei, O. Munteshari, J. Lau, B. Dunn and L. Pilon, *J. Phys. Chem. C*, 2018, **122**, 194–206.
44 C. H. Hsu and F. Mansfeld, *Corrosion*, 2001, **57**, 747–748.
45 G. J. Brug, A. L. G Van Den Eeden, M. Sluyters-rehbach and J. H. Sluyters, *J. Electroanal. Chem.*, 1984, **176**, 275–295.
46 B. Hirschorn, M. E. Orazem, B. Tribollet, V. Vivier, I. Frateur and M. Musiani, *J. Electrochem. Soc.*, 2010, **157**, C452.
47 M. E. Orazem, I. Frateur, B. Tribollet, V. Vivier, S. Marcelin, N. Pébère, A. L. Bunge, E. A. White, D. P. Riemer and M. Musiani, *J. Electrochem. Soc.*, 2013, **160**, C215–C225.
48 A. Allagui, H. Alawadhi, M. Alkaaby, M. Gaidi, K. Mostafa and Y. Abdulaziz, *Phys. Status Solidi A*, 2016, **213**, 139–145.
49 X. G. Zhang, *Electrochemistry of Silicon and its Oxide*, Springer, Boston, MA, 2001.
50 S. Tengeler, Cubic Silicon Carbide For Direct Photoelectrochemical Water Splitting, PhD thesis, Grenoble Alpes University, France, 2017.
51 P. Deimel and F. Allegretti, *ELECTRON SPECTROSCOPY of SURFACES Elemental and Chemical Analysis with X-Ray Photoelectron Spectroscopy*, 2016.
52 A. P. Hitchcock, in *Volume II of Handbook of Nanoscopy*, ed. G. Van Tendeloo, D. Van Dyck and S. J. Pennycook, 2012, ch. 22.
53 J. Deng, Q. Zhang, X. Lv, D. Zhang, H. Xu, D. Ma and J. Zhong, *ACS Energy Lett.*, 2020, **5**, 975–993.
54 R. Belkhou, S. Stanescu, S. Swaraj, A. Besson, M. Ledoux, M. Hajlaoui and D. Dalle, *J. Synchrotron Radiat.*, 2015, **22**, 968–979.
55 S. Shen, J. Zhou, C. L. Dong, Y. Hu, E. N. Tseng, P. Guo, L. Guo and S. S. Mao, *Sci. Rep.*, 2014, **4**, 6627.

56 L. Vayssieres, J. Guo and J. Nordgren, *J. Nanosci. Nanotechnol.*, 2001, **1**, 385–388.
57 Z. Fu, T. Jiang, Z. Liu, D. Wang, L. Wang and T. Xie, *Electrochim. Acta*, 2014, **129**, 358–363.
58 A. F. Gualtieri and P. Venturelli, *Am. Mineral.*, 1999, **84**, 895–904.
59 R. M. Cornell and U. Schwertmann, *Introduction to the Iron Oxides*, Wiley-VCH Verlag, 2003.
60 K. M. Peterson, P. J. Heaney and J. E. Post, *Powder Diffr.*, 2018, **33**, 287–297.
61 C. Frandsen, B. A. Legg, L. R. Comolli, H. Zhang, B. Gilbert, E. Johnson and J. F. Banfield, *CrystEngComm*, 2014, **16**, 1451–1458.
62 J. Baumgartner, A. Dey, P. H. H. Bomans, C. Le Coadou, P. Fratzl, N. A. J. M. Sommerdijk and D. Faivre, *Nat. Mater.*, 2013, **12**, 310–314.
63 V. M. Yuwono, N. D. Burrows, J. A. Soltis and R. Lee Penn, *J. Am. Chem. Soc.*, 2010, **132**, 2163–2165.
64 Y. Niu, Y. Zhou, P. Niu, H. Shen and Y. Ma, *J. Nanosci. Nanotechnol.*, 2019, **19**, 3437–3446.
65 S. I. Yi, Y. Liang, S. Thevuthasan and S. A. Chambers, *Surf. Sci.*, 1999, **443**, 212–220.
66 B. Zhao, T. C. Kaspar, T. C. Droubay, J. McCloy, M. E. Bowden, V. Shutthanandan, S. M. Heald and S. A. Chambers, *Phys. Rev. B: Condens. Matter Mater. Phys.*, 2011, **84**, 1–9.
67 J. F. Moulder, W. F. Stickle, P. E. Sobol and K. D. Bomben, *Handbook of X-Ray Photoelectron Spectroscopy*, Perkin-Elmer Corporation, Minnesota, 1992.
68 B. L. Henke, E. M. Gullikson and J. C. Davis, *At. Data Nucl. Data Tables*, 1993, **54**, 181–342.
69 C. Le Guillou, S. Bernard, F. De La Pena and Y. Le Brech, *Anal. Chem.*, 2018, **90**, 8379–8386.
70 I. N. Koprinarov, A. P. Hitchcock, C. T. McCrory and R. F. Childs, *J. Phys. Chem. B*, 2002, **106**, 5358–5364.
71 F. M. F. de Groot, M. O. Figueiredo, M. J. Basto, M. Abbate, H. Petersen and J. C. Fuggle, *Phys. Chem. Miner.*, 1992, **19**, 140–147.
72 R. Laskowski and P. Blaha, *Phys. Rev. B: Condens. Matter Mater. Phys.*, 2010, **82**, 1–6.
73 M. Wu, H. L. Xin, J. O. Wang, X. J. Li, X. B. Yuan, H. Zeng, J. C. Zheng and H. Q. Wang, *J. Synchrotron Radiat.*, 2018, **25**, 777–784.
74 F. Frati, M. O. J. Y. Hunault and F. M. F. De Groot, *Chem. Rev.*, 2020, **120**, 4056–4110.
75 J. G. Chen, *Surf. Sci. Rep.*, 1997, **30**, 1–152.
76 F. M. F. de Groot, M. Grioni and J. C. Fuggle, *Phys. Rev. B*, 1989, **40**, 5715–5723.
77 G. S. Henderson, F. M. F. De Groot and B. J. A. Moulton, *Rev. Mineral. Geochem.*, 2014, **78**, 75–138.
78 D. K. Bora, A. Braun, S. Erat, A. K. Ariffin, R. Löhnert, K. Sivula, J. Töpfer, M. Grätzel, R. Manzke, T. Graule and E. C. Constable, *J. Phys. Chem. C*, 2011, **115**, 5619–5625.
79 A. Braun, K. Sivula, D. K. Bora, J. Zhu, L. Zhang, M. Grätzel, J. Guo and E. C. Constable, *J. Phys. Chem. C*, 2012, **116**, 16870–16875.
80 Y. Ye, J. E. Thorne, C. H. Wu, Y. S. Liu, C. Du, J. W. Jang, E. Liu, D. Wang and J. Guo, *J. Phys. Chem. B*, 2018, **122**, 927–932.
81 E. C. Todd, D. M. Sherman and J. A. Purton, *Geochim. Cosmochim. Acta*, 2003, **67**, 881–893.
82 F. Brandt, T. Schäfer, F. Claret and D. Bosbach, *Chem. Geol.*, 2012, **329**, 42–52.
83 C. X. Kronawitter, I. Zegkinoglou, C. Rogero, J. H. Guo, S. S. Mao, F. J. Himpsel and L. Vayssieres, *J. Phys. Chem. C*, 2012, **116**, 22780–22785.
84 B. Gilbert, C. Frandsen, E. R. Maxey and D. M. Sherman, *Phys. Rev. B: Condens. Matter Mater. Phys.*, 2009, **79**, 1–7.
85 C. X. Kronawitter, J. R. Bakke, D. A. Wheeler, W. C. Wang, C. Chang, B. R. Antoun, J. Z. Zhang, J. Guo, S. F. Bent, S. S. Mao and L. Vayssieres, *Nano Lett.*, 2011, **11**, 3855–3861.
86 Y. Ye, M. Kapilashrami, C. H. Chuang, Y. S. Liu, P. A. Glans and J. Guo, *MRS Commun.*, 2017, **7**, 53–66.
87 H. Gerischer, in *Advances in electrochemistry and electrochemical engineering*, ed. P. Delahay and C. Tobias, Interscience, New-York, 1961, vol 1, pp. 4:139–232.
88 H. Gerischer and A. Heller, *J. Phys. Chem.*, 1991, **95**, 5261–5267.
89 M. Li, T. Liu, Y. Yang, W. Qiu, C. Liang, Y. Tong and Y. Li, *ACS Energy Lett.*, 2019, **4**, 1983–1990.
90 J. W. Jang, C. Du, Y. Ye, Y. Lin, X. Yao, J. Thorne, E. Liu, G. McMahon, J. Zhu, A. Javey, J. Guo and D. Wang, *Nat. Commun.*, 2015, **6**, 1–5.